LAWRENCE
LIVERMORE
NATIONAL
LABORATORY

# Thermal Studies of the Laser Inertial Fusion Energy (LIFE) Target during Injection into the Fusion Chamber

R. R. Miles, M. Havstad, M. LeBlanc, A. Chang, I. Golosker, P. Rosso

September 9, 2014

**Disclaimer**

This document was prepared as an account of work sponsored by an agency of the United States government. Neither the United States government nor Lawrence Livermore National Security, LLC, nor any of their employees makes any warranty, expressed or implied, or assumes any legal liability or responsibility for the accuracy, completeness, or usefulness of any information, apparatus, product, or process disclosed, or represents that its use would not infringe privately owned rights. Reference herein to any specific commercial product, process, or service by trade name, trademark, manufacturer, or otherwise does not necessarily constitute or imply its endorsement, recommendation, or favoring by the United States government or Lawrence Livermore National Security, LLC. The views and opinions of authors expressed herein do not necessarily state or reflect those of the United States government or Lawrence Livermore National Security, LLC, and shall not be used for advertising or product endorsement purposes.

This work performed under the auspices of the U.S. Department of Energy by Lawrence Livermore National Laboratory under Contract DE-AC52-07NA27344.

# Thermal Studies of the Laser Inertial Fusion Energy (LIFE) Target during Injection into the Fusion Chamber

Miles, R., Havstad, M., LeBlanc, M., Chang, A., Golosker, I., Rosso, P.

## 1.0 Introduction

The Laser Inertial Fusion Energy (LIFE) commercial electrical generating plant was conceptualized at LLNL [1-1]. Like many inertial fusion energy (IFE) plant concepts[1-2,1-3], the target is expected to be injected into the fusion chamber at repetition rates of 5-20 per second and velocities of about 250 m/s. During the ~100 ms injection acceleration and flight time into chamber-center where implosion occurs, the target experiences intense heat fluxes to its surfaces. During injection, the target experiences frictional heating if the injector is a gas gun or $I^2R$ energy from currents induced in the hohlraum if induction acceleration is used. The target also experiences convective heating from the hot chamber gases and infrared (IR) radiation heating from the chamber walls. Implosion will be unsuccessful if the target components lose structural integrity (e.g. melt) or the DT overheats inhibiting successful compression of the fuel. This study looks at the thermal profile of the LIFE target as it is injected into the fusion chamber to ensure a target design which meets the thermal requirements for successful implosion at chamber center.

The candidate LIFE target is shown in Figure 1-1 [Ref. 1-4, 1-5]. The LIFE target is an indirect drive target consisting of a hollow spherical capsule with a diamond ablator and an inner layer of solid DT held in the center of a lead hohlraum by two <100 nm thick carbon-composite capsule support membranes. A ~500 nm thick polyimide LEH window seals each axial end of the target. A 500 nm thick polyimide membrane coated with ~30 nm of aluminum serves as the IR shield and support for the lead P2 shield which is ~5mm in diameter and ~ 200 um thick. Helium at a density of ~1 mg/cc at ~18K fills the target.
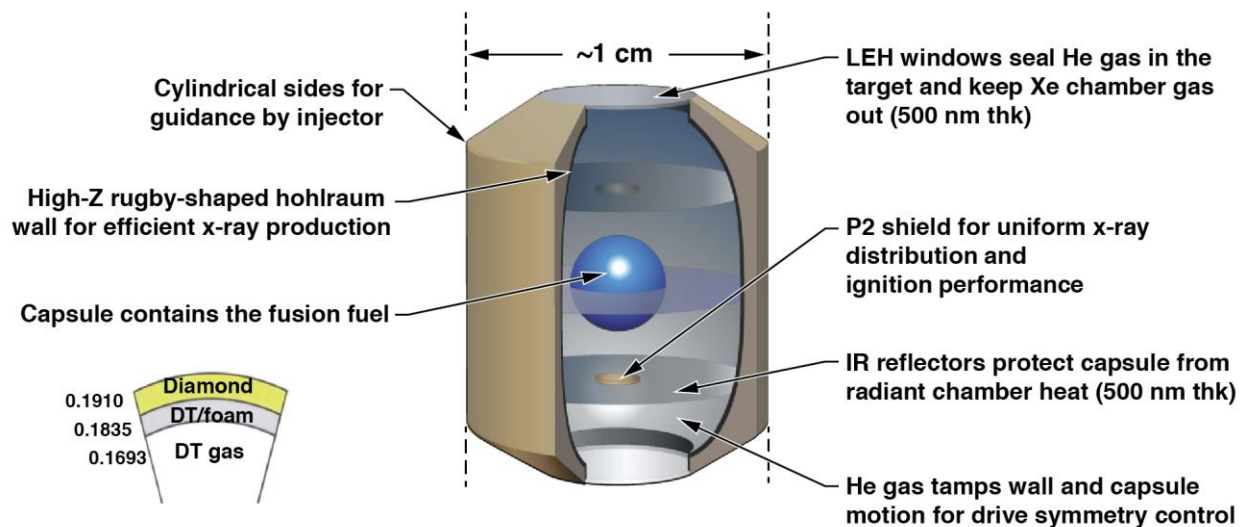


*Figure 1-1. LIFE target design*

As shown in Figure 1-2, the target experiences three phases of environmental conditions during the injection process.  The first phase is the acceleration injection phase during which time the target is accelerated up to its flight velocity by the injector.  The injector mechanism has not been specified but leading candidates include a gas gun and an induction accelerator.  During this time, the target hohlraum could be subjected to external thermal loads resulting from the hot gas of a gas gun, possible friction with the injector barrel or induced electrical $I^2R$ heating.  The second phase is called the drift phase named for the drift through the gas between the muzzle of the injector and the inner chamber wall.  Lastly, the target flies through the chamber to chamber-center where implosion occurs.  The chamber contains low density (~6 ug/cc), hot (~6000K) xenon gas.  The chamber walls are hot (~900K) and emit infrared radiation though the target laser entrance hole (LEH) window.  The flight times through each phase of the target flight are ~42 ms in the injector, ~16 ms in the drift region and ~24 ms in the chamber which yields a total flight time of ~82 ms.   Beyond the obvious requirement to maintain structural integrity (i. e. no softening or melting) during flight, the primary thermal requirement of the target is derived from the desire to limit the increase in vapor pressure of the DT beyond a point where implosion would be inhibited due to back-pressure during implosion. Max Tabak estimated that this represented a requirement for a temperature increase of no more than 0.1 K at the surface of the DT layer.  While this numerical requirement needs to be reconsidered in more detail, we used this as the assumed requirement for this analysis. In essence, the capsule is thermally protected using the hohlraum and the IR shields as barriers to heat transfer and by limiting the exposure time.
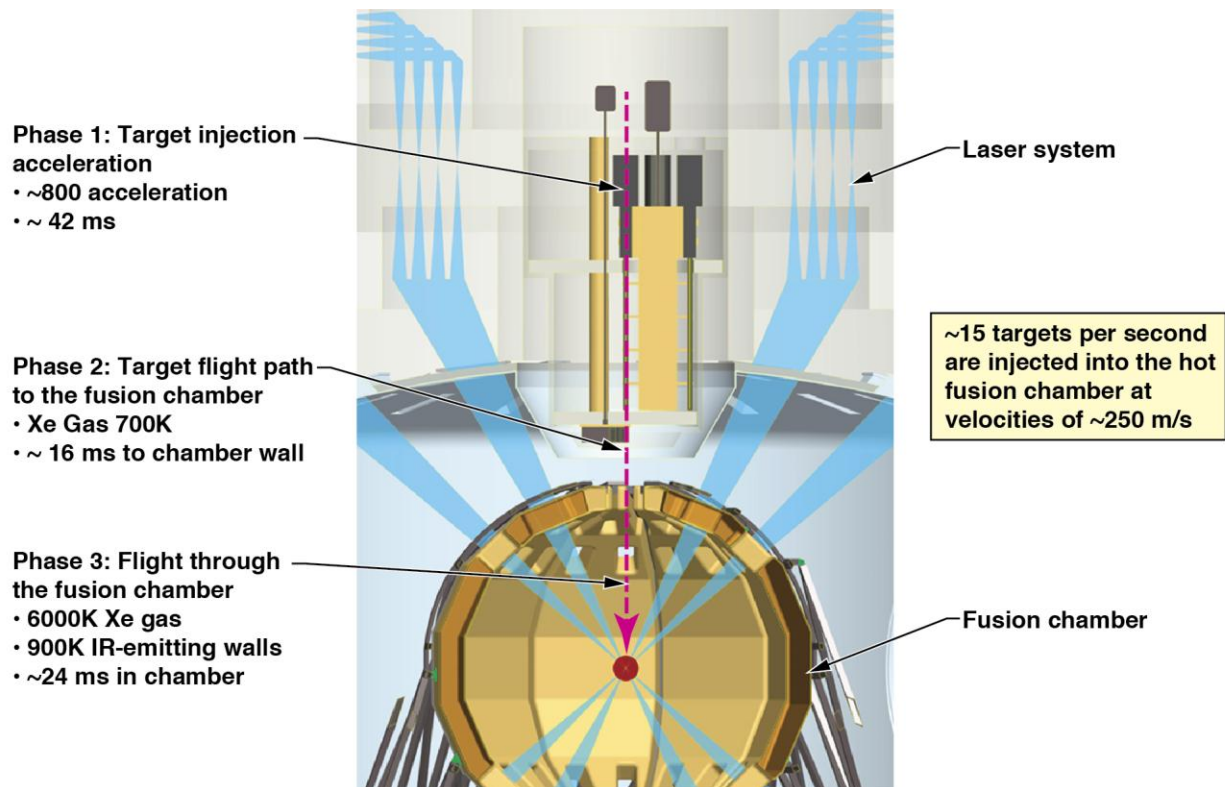


*Figure 1-2. Schematic of LIFE target flight into the fusion chamber*

To determine whether or not a LIFE target would survive the injection process, a series of analytical models were developed. The results of this work were published in reference 1-6.  This document discusses tests which were conducted to validate the results of this analysis.  The tests were not conducted in the extreme environmental conditions expected in a fusion chamber due the difficultly of duplicating these conditions but were used to emulate essential aspects of the heat transfer phenomena.  This task consists of measuring the convection heat transfer coefficients internal and external to the target and the parameters of radiative heat transfer.

### 1.1 Thermal models of the target in the LIFE plant

The results of the modeling efforts for flight into the fusion chamber are summarized in Figures 1-3 and 1-4 and in Table 1-1 below.  The major ingresses of heat into the target are heat absorbed by the hohlraum during the process of injection acceleration and convective heat from the chamber gasses to the thin LEH window which heats the helium behind the window establishing convection currents which in turn heat the capsule.  The injection-acceleration heat source is a lower intensity source than the chamber heat source but has a longer period of time to penetrate through the hohlraum and migrate towards the capsule.  The hohlraum acts as a heat sink for the intense heat of the chamber.  Nearly all the IR radiation from the chamber walls is reflected off the IR shield.  The heat transfer coefficient at the LEH window can be reduced by adding a cup geometry in front of the LEH window which creates a stagnation region as shown in Figure 1-4.  At some target velocities the specification of a maximum temperature increase of 0.1 K increase at the DT inner surface  will be exceeded unless stronger measures are taken to reduce the heat absorbed at the LEH window by, for example, adding a 10 um solid methane sublimation layer to the window.  In either case, the heating of the helium behind the LEH window increases the internal helium pressure in the adjacent compartment to such a degree that rupture of the LEH window and IR shield would result were the pressure not relieved by adding by-pass ports around the IR shield to vent the gas from the first compartment near the LEH window into the second compartment near the capsule.  Although this increases the temperature in the second compartment by some small degree, the gas is largely cooled by the hohlraum as it is vented, reducing the thermal threat to the capsule.
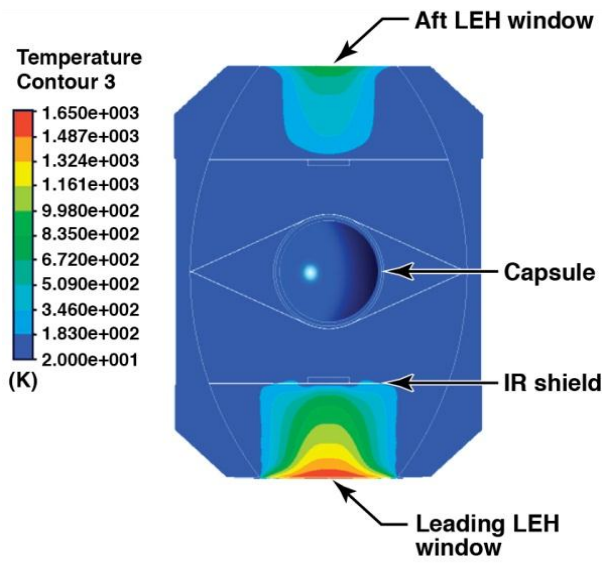
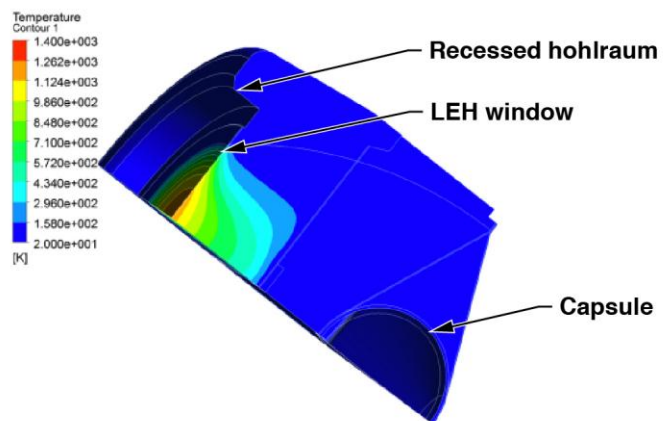*Figure 1-3. Thermal distribution in target at chamber center*



*Figure 1-4. Thermal distribution in target with recessed leading edge at chamber center*

**Table 1-1. Summary of thermal analysis for a variety of cases (Initial target temperature is 20K)**

| Case No. | | LEH average temperature (K) | He front compartment average temperature (K) | He front compartment pressure change (Pa) | P2 shield average temperature (K) | He second compartment average temperature (K) | He second compartment pressure change (Pa) | Capsule ablator max. temperature (K) | DT inner surface max temperature (K) |
|---|---|---|---|---|---|---|---|---|---|
| 1 | Baseline (rugby) case w/ frictional heating during injection | 1268 | 315 | 111896 | 59.5 | 42.2 | 21991 | 22.4 | 20.3 |
| 2 | Baseline case w/o frictional heating during injection but with 700 K gas environment instead | 1275 | 312 | 99052 | 58.6 | 40.7 | 18836 | 22.4 | 20.26 |
| 3 | above case but switch design to recess LEH | 563 | 199 | 71078 | 37.1 | 29.7 | 11910 | 20.4 | 20.08 |
| 4 | Add helium bypass flow to above | 580 | 90.7 | 23021 | 36.6 | N/A | N/A | 20.6 | 20.08 |
| 5 | Baseline with phase change material(methane) | 72.9 | 38.5 | 26603 | 22.8 | NR | NR | 20.4 | 20.03 |
| 6 | Baseline with phase change material (pentane) | 245 | 83.6 | 56922 | 30.2 | NR | NR | 20.2 | 20.04 |
| 7 | helium bypass with recess LEH and phase change material (pentane) | 245 | 49 | 23363 | 26.7 | N/A | N/A | 20.3 | 20.05 |
| 8 | Baseline case w/ frictional heating during injection but 150m/s | 1160 | 296 | 105161 | 64.2 | 43.1 | 22808 | 22.7 | 20.37 |
| 9 | Helium bypass, recessed LEH window, no friction, 300K gas with 150 m/s | 520 | 87.5 | 25468 | 40.9 | N/A | N/A | 20.8 | 20.15 |
| 10 | Baseline with phase change material (pentane) but 300K gas, 150 mps | 245 | 85 | 56444 | 35.9 | 28.5 | 12806 | 21 | 20.14 |
| 11 | Baseline with phase change material (methane) but 300K gas, 150 mps | 73 | 39.7 | 27882 | 26.3 | 25.2 | 9230 | 20.5 | 20.07 |
| 12 | Baseline but 420K gas, 200 mps | 1224 | 302.6 | 97381 | 56.3 | 40.4 | 18589 | 22.3 | 20.25 |
| 13 | baseline but adiabatic LEH, all time | 30.75 | 25.7 | 9880 | 20.4 | NR | NR | 20.3 | 20.03 |

## 1.2 Tests

Three sets of experimental tests were pursued. These tests were used to 1) measure the heat transfer coefficient on the external surface of the target subjected to chamber gas 2) verify the existence of convection currents internal to the target and measure the internal heat transfer coefficients between the LEH window and the helium target gas and 3) measure the absorption, reflectance and transmittance of IR radiation through the IR shield and carbon-composite membrane. In each case, the relevant heat transfer elements were emulated and the test conditions modeled. The expectation is that agreement between the model and the test results will increase the confidence in the model of the target flight in the chamber.

## 1.3 References

1-1 Latkowski, J. F. et. al., "Chamber Design for the Laser Inertial Fusion-based Energy (LIFE) Engine," *Fusion Science and Technology,* **60**, 54 (2011).

1-2 Meier, W. R. et. al., "OSIRIS and SOMBRERO Inertial Confinement Fusion Power Plant Designs: Volume 1 Executive Summary and Overview," WSJA-92-01, DOE/ER/54100-1 (1992).

1-3 Sethan, J. D. et. al., "Fusion Energy with Lasers, Direct-drive Targets, and Dry Wall Chambers," *Nuclear Fusion*, **43**, 1693 (2003).

1-4 Amendt, P., et. al., "LIFE Pure-Fusion Target Designs: Status and Future," *Fusion Science and Technology,* **60**, 49, (2011).

1-5 Miles, R., et. al,. "Challenges Surrounding the Injection and Arrival of Targets at LIFE Fusion Chamber Center," *Fusion Science and Technology,* **60**, 61 (2011).

1-6 Miles, R., et. al. "Thermal and Structural Issues of Target Injection into a laser-Driven Inertial Fusion Energy Chamber", *Fusion Science and Technology*, 66, Oct 2014.

**2.0 Measurement of the external heat transfer coefficient**

The objective of the external heat transfer coefficient section was to validate the models for the external heat transfer conditions as best as possible given that the exact fusion chamber environment cannot be easily reproduced.  The test was conducted using a flow of gas through a pipe into which a dummy target was placed with external dimensions similar to the actual LIFE target as shown in the diagram of Figure 2-1.  Initially, heated nitrogen gas (~700K) was forced over the target while the gas temperature and target surface temperatures were measured so that the heat transfer coefficient could be calculated from the difference of these temperatures over time according to Equation 2-1 in Section 2.2.  The pressure of the gas in the pipe was low, ~23 torr, similar to that expected in the fusion chamber.  Originally we planned to heat the gas flowing through the pipe.  Unfortunately, the heater broke before good data was obtained so the test was reversed.  The target was pre-heated to temperatures of about 865 K then ambient air was drawn over the dummy-target and the heat transfer coefficient was measured by the difference in temperature between the gas temperature and the surface temperature of the target.   The gas pressure was about 23 torr and the gas velocity was about 25 m/s.

*2.1 Test set-up*

A photograph of the external view of the test set-up is shown in Figure 2-2.  The dummy target was suspended off a cantilevered tube which contained the thermocouples used to measure the surface temperature is shown in Figures 2-3 and 2-4.  The dummy test target is comprised of a hollow macor shell with holes drilled to permit the insertion of thermocouples through the inner core, through the drilled holes and mounted flush with the shell surface as shown in Figures 2-4 and 2-5.  Thermocouples used to measure the gas temperature were held with a supporting rod as shown in Figures 2-3 and 2-4.  A clam-shell heater was wrapped around the flow tube and was used to heat the apparatus to its initial temperature of about 865K prior to  the gas flow.   A vacuum pump pulled ambient air through the critical orifice located at the inlet of the flow tube.  Since the flow was choked as it traversed the critical orifice, the flow rate was dependent on the upstream pressure, in this case, atmospheric pressure.  The flow rate through the flow tube was measured by the Bernoulli's differential pressure technique between the static and dynamic pressures.
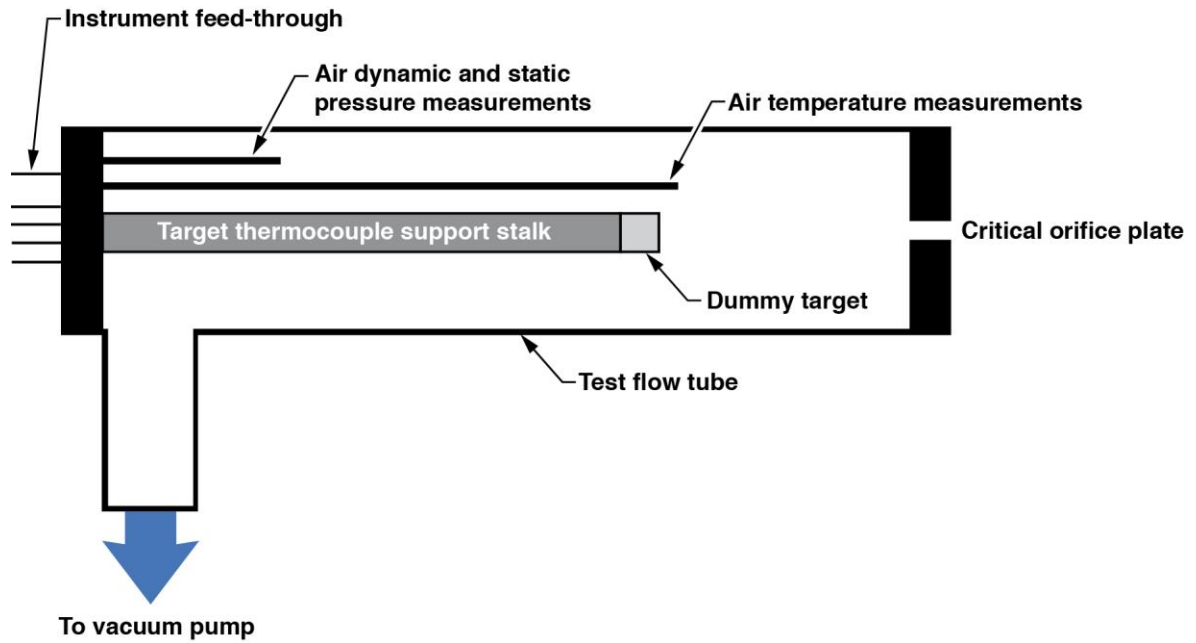
*Figure 2-1. Schematic for test 2 set-up to measure external heat transfer coefficient*
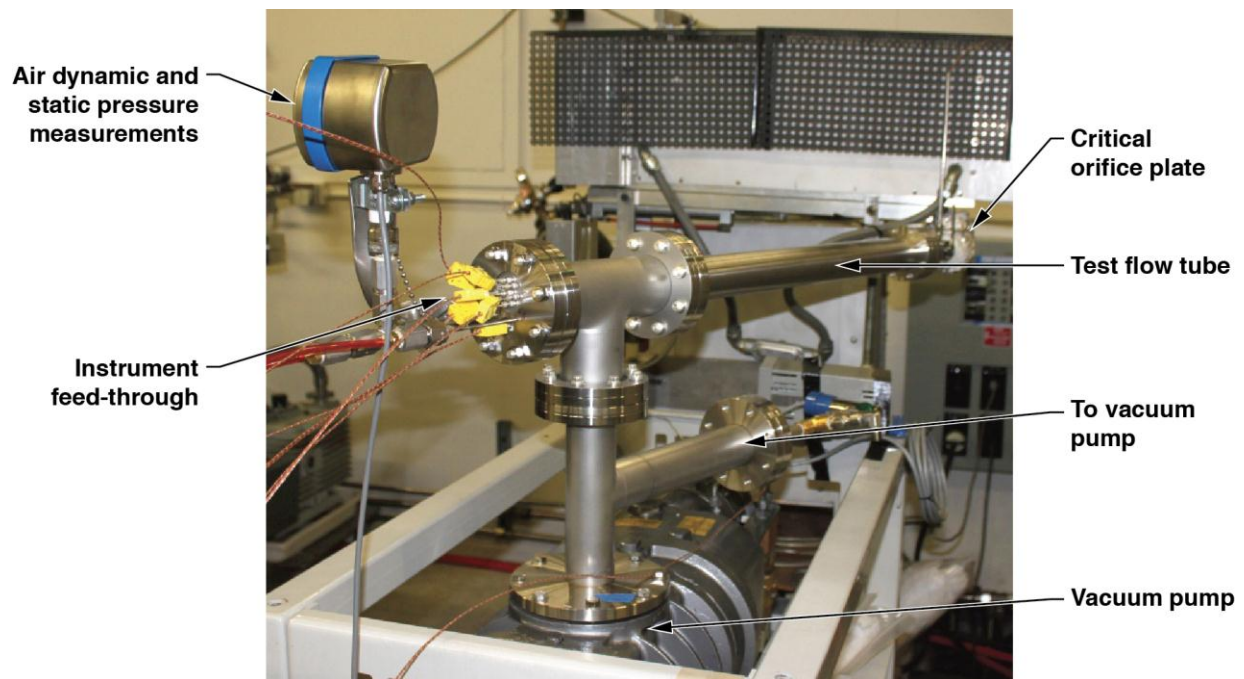


*Figure 2-2. Picture of test setup used to measure the external heat transfer coefficient of the target*
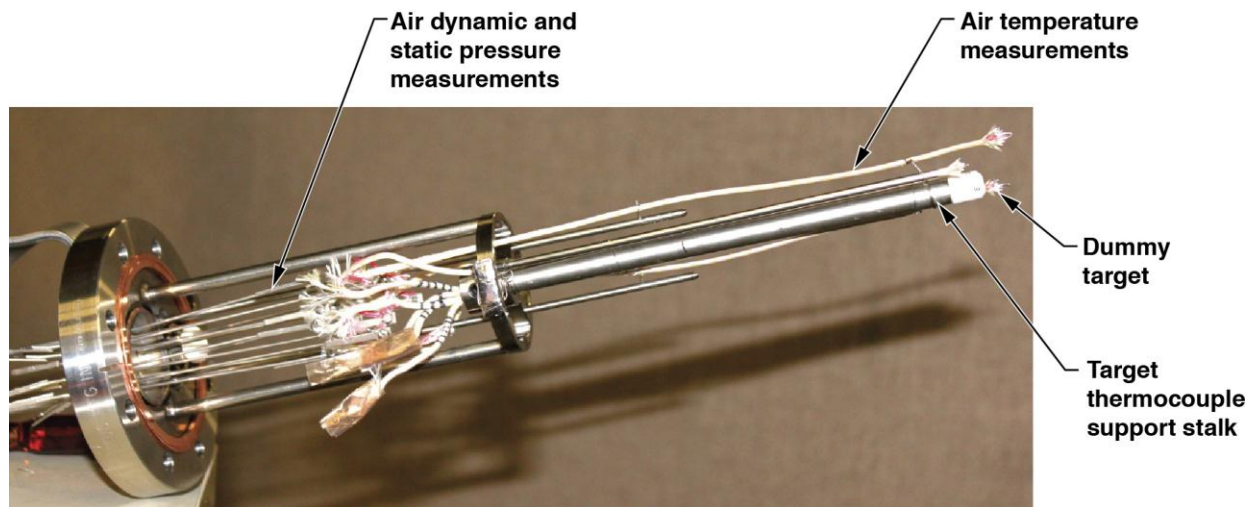
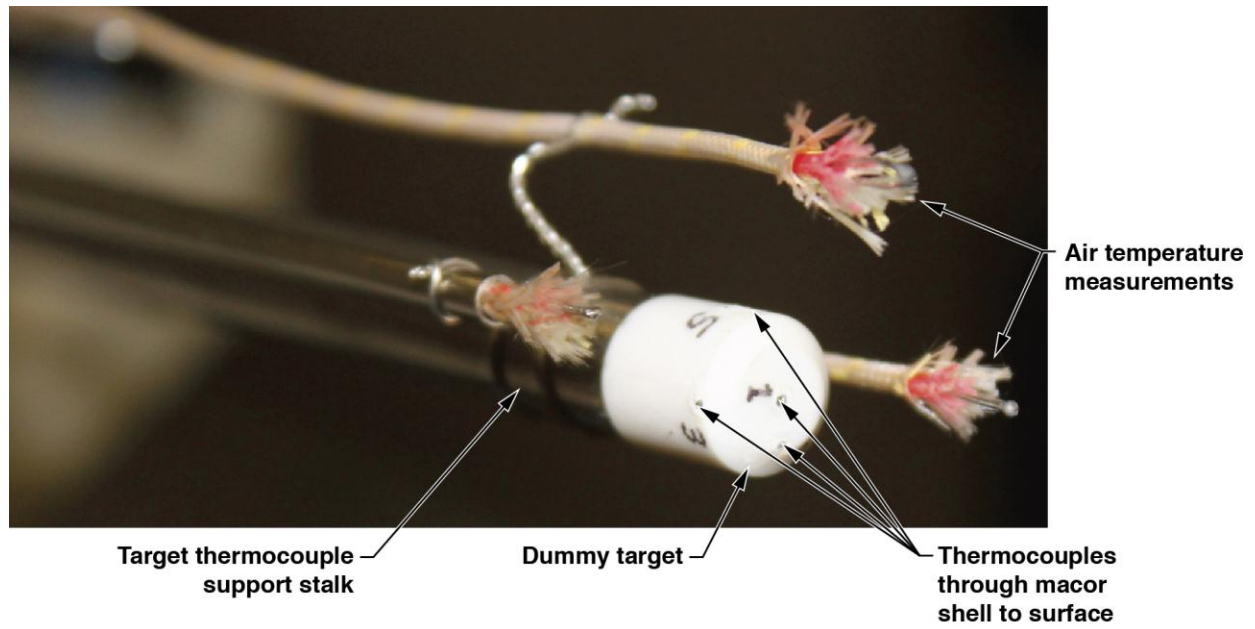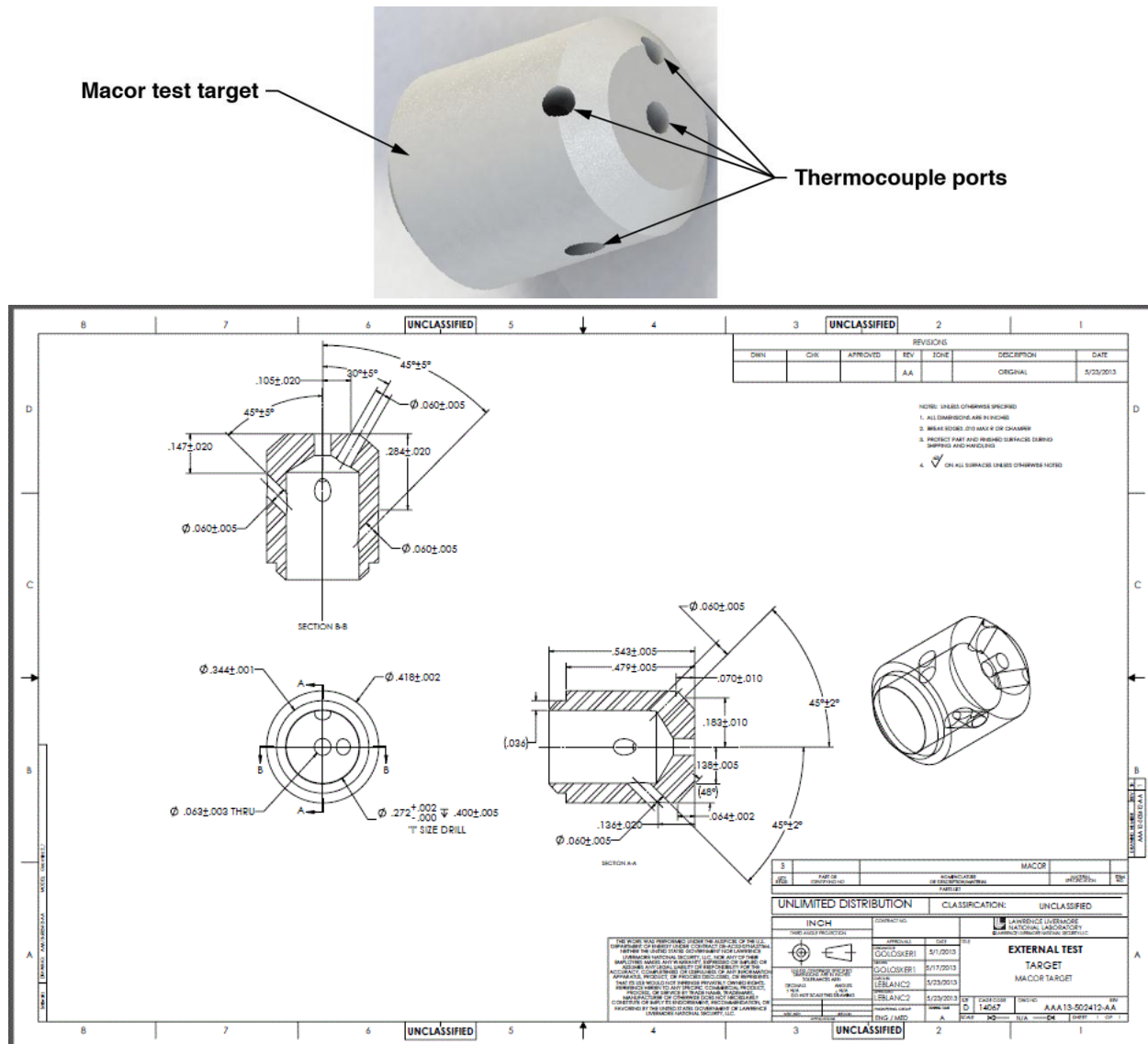*Figure 2-3. Dummy target assembly for external heat transfer coefficient measurements*



*Figure 2-4. Close-up of dummy target for heat transfer coefficient measurements*

Macor test target

Thermocouple ports



*Figure 2-5. Test target model and drawing*

## *2.2 Analytical model results*

Analytical models were used to predict the heat transfer coefficient in both the fusion chamber and in the test used to validate the models.  For the Reynolds and Mach numbers of interest here there are five published heat transfer correlations of greatest interest. These are Belov and Terpigor'ev [2-1] (for the stagnation zone), Sogin [2-2] (for the rear face of the target), Hadad and Jafarpur [2-3] (an average over the body), Kang and Sparrow [2-4] (for the cylindrical outer face) and Na and Pop [2-5] (for the cylindrical face again but here varying along the face).  These correlations have compared well to our CFD work concerning the target flight under the planned use conditions, as shown in Figure 2-5 below.
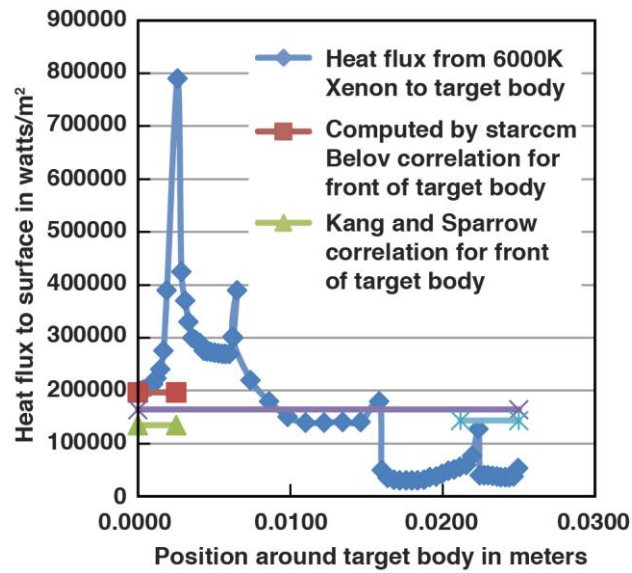
*Figure 2-6. Comparison of CFD and correlations for target flight under planned use (fusion chamber) conditions*

The fluid flow field around the target for a heat flux similar to that given in Figure 2-6 is shown below in Figure 2-7.
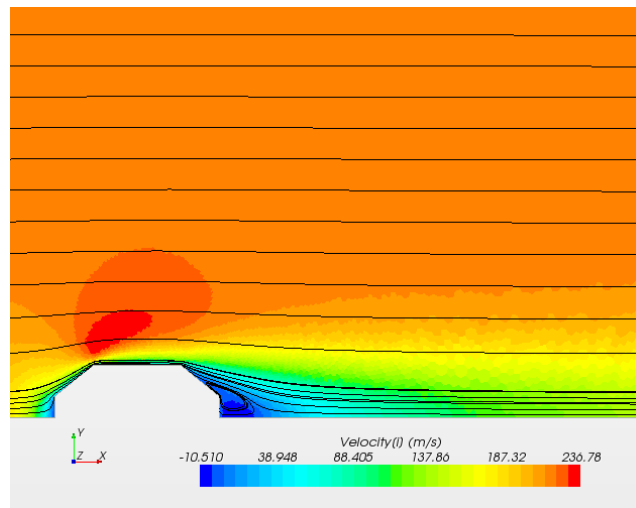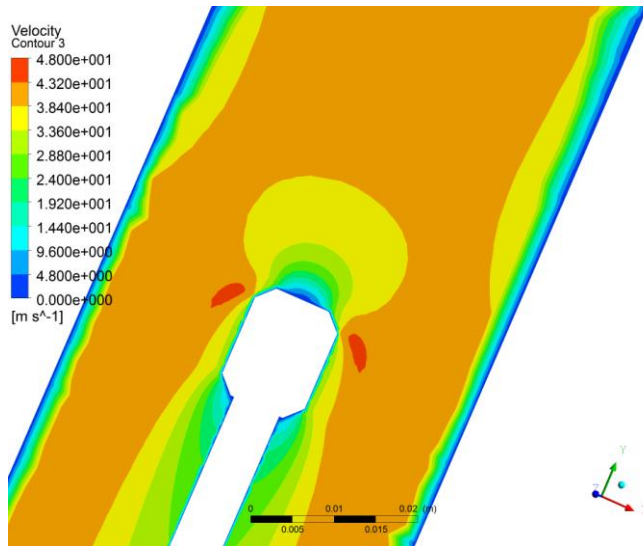


*Figure 2-7. Streamlines and contours of velocity for flow around the target under expected use (fusion chamber) conditions*

Simulations of flow around the test body at expected test conditions (Figure 2-8) correlate well to that shown for target under use (fusion chamber) conditions (Figure 2-7).

*Figure 2-8. Contours of velocity for flow around the test body for expected test conditions*

Both figures show the acceleration in flow around the front corners of the body where we expect high heat transfer coefficients. The frontal stagnation zones are similar between the test and planned use and the front portions of the flow fields outside the cylindrical body portion of the target are well matched. The necessity to remove instrumentation wires out the back end of the dummy target assembly made the rear of the flow field different in the test case than in the case of flight through the fusion chamber.

Of particular interest to data reduction is the transient response of the target shell for use (fusion chamber) and test.  Figures 2-9 and 2-10 below show thermal profiles in the fusion target shell and test body shell after 15 seconds of exposure to convective heating as expected in test. Though the planned target exposure in the fusion chamber is only on the order of 0.080 sec, it is interesting to see both the fusion target and the test target have small thermal gradients through the hohlraum wall for the planned test exposure. The small gradients in the test body shell (macor rather than lead) mean that data reduction assuming negligible thermal gradients locally in the macor shell may be adequate.
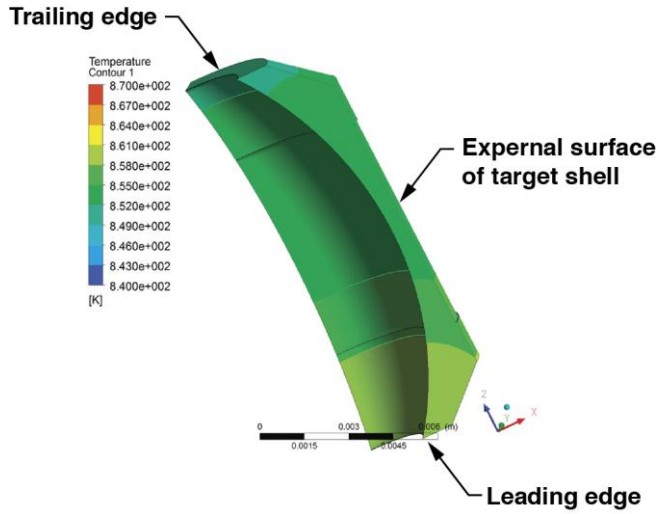
*Figure 2-9. Thermal gradients in a target shell exposed to 15 Seconds of test body heating by convection*
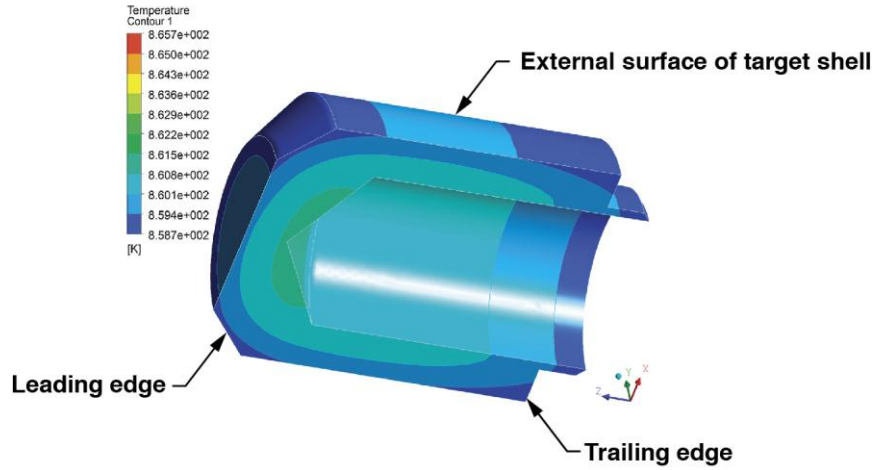


*Figure 2-10.  Thermal gradients in a test body shell exposed to 15 seconds of test body heating by convection*

Analysis of the tests begins with a transient heat transfer equation:

$$\rho_{bd}C_{bd}V_{bd}\frac{dT_{bd}}{dt} = h(T_\infty - T_{bd})A_{bd} - k_c(T_{bd} - T_m)A_c/\Delta x \qquad \text{(Equation 2-1)}$$

Here bd can denote the target body (the macor shell in the test apparatus) or merely the thermocouple bead.   The variables are:  $\rho$ Is density , C is thermal capacity, V is the body volume, h is the heat transfer coefficient, T is the temperature, t is time, A is the area over with the heat flux is applied and x is the

thickness.  The subscripts are    $\infty$ for the mid air stream, c for the target and m for the target interior.

13

The conduction term on the right can represent the conductive heat loss from the thermocouple wires leaving the sensing bead or it can represent the thermal losses from the macor shell to its internal void volume. The transient simulation shown above in Figure 2-10 was done in two ways, first with the internal surfaces of the macor shell were set to an adiabatic boundary condition and second with a modest free convection loss coefficient of 10 w/m$^2$K applied to the inside surface. The transient responses of the volume average of temperature for the macor shell for the two cases are shown in Figures 2-11 and 2-12 below. The similarity in the two figures confirms that for the conditions and time scales of interest to the tests, convective losses to the test shell interior can be neglected.
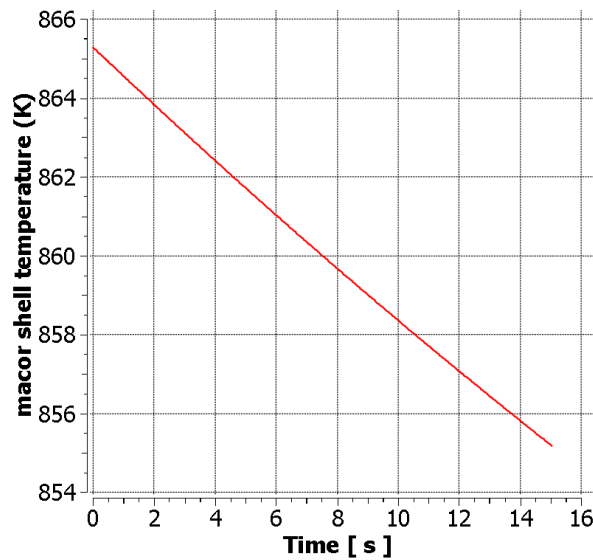
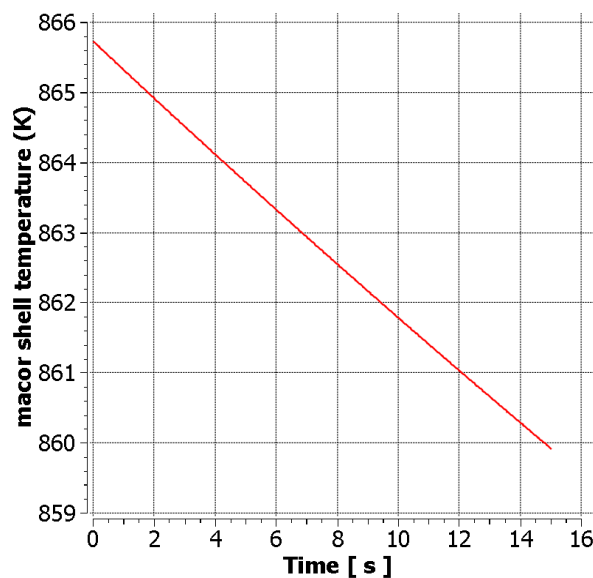Figure 2-11. Thermal transient of test shell for adiabatic shell interior

Figure 2-12. Thermal transient of test shell with modest heat loss to shell

14

Examining thermal gradient effects at a thermocouple bead embedded in a macor shell is useful. Figure 2-13 shows thermal gradients in a bead bonded to macor subjected to transient test conditions. The higher thermal conductivity of the bead coupled with its size (about half the macor shell thickness) makes it something of a thermal short towards the interior of the macor shell.
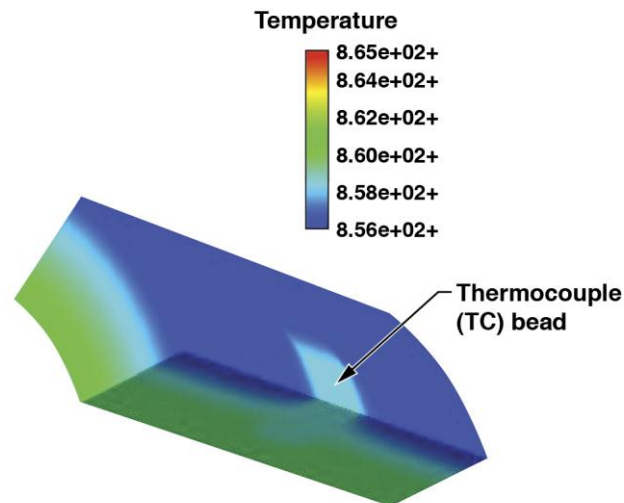


*Figure 2-13. Thermal profile (at time= 8 seconds) of a chromel-alumel thermocouple bead embedded in a cylindrical macor shell subjected to test conditions*

The TC bead (blue square on surface of Figure 2-13) is measuring an average of the macor temperature profile. Transient thermal effects in the test are better understood by comparing the thermal response of several items from this simulation. Figure 2-14 shows a simulated macor and TC bead local and average temperatures of interest of the key first 8 seconds of the tests.
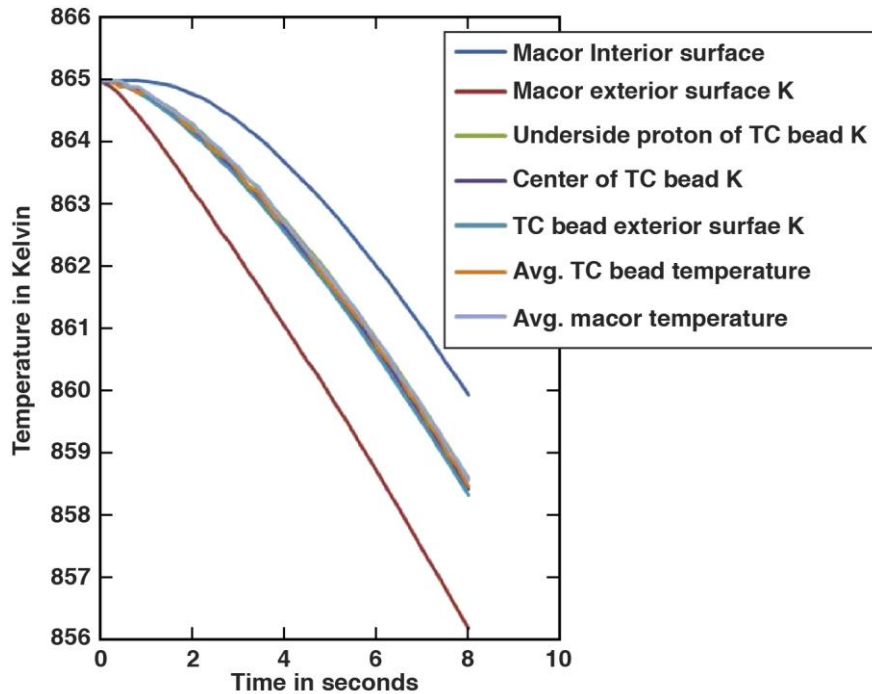
*Figure 2-14. Modeled transient temperatures for macor and thermocouple bead subjected to test*

The thermocouple is not measuring the macor surface temperature or its interior temperature. Temperature gradients within the metal TC bead are small and the average bead temperature follows the local average macor temperature quite well (bead response varies with location on the macor shell in the test data). Thus test data will be analyzed with the transient heat transfer equation given above, while neglecting the heat loss term to the interior and defining bd as the thermocouple bead.

The Belov and Terpigor'ev correlation, simplified for use here takes the form:

$$Nu = \frac{hD}{k} = CRe^{n(Re)}Pr^{n(Pr)} \qquad \text{(Equation 2-2)}$$

The symbols are: Nu is the Nusselt number, h is the heat transfer coefficient, k is the thermal conductivity of the gas, D is the object diameter, C and n are constants, Re is the Reynold's number, Pr is the Prandlt number. The other cited works have mostly similar forms of this equation with differing values for the exponents. When we apply this correlation to both planned target use in the fusion chamber and our test conditions described above we get moderately different results for the convective heat transfer coefficient, h. Test and use heat transfer coefficients and other conditions for the stagnation point are compared in Table 2-1 below. So while the test conditions differ from the planned use fusion conditions, the measured heat transfer coefficients are comparable.

**Table 2-1. Comparison of conditions at the stagnation point**

| | Planned use | Test | Item |
|---|---|---|---|
| | stag. Pt. | stag. Pt. | units |
| Surface Temperature | 20 | 800 | K |
| Gas Temperature | 6000 | 800 | K |
| Gas pressure | 3040 | 4400 | Pa |
| Gas molec weight | 131 | 29 | kg/kmol |
| Prandtl | 0.8 | 0.76 | - |
| Reynolds | 280 | 270 | - |
| Nu | 12 | 9 | - |
| h | 31 | 40 | w/(m2K) |
| mach | 0.31 | 0.044 | - |

The heat transfer coefficient can be calculated using the constants found in the other cited works as shown in Table 2-2 below, where the fluid properties have been evaluated at the "film" values, the average of the surface and free stream temperatures similar to Table 2-1. The range of possible heat transfer coefficients is shown in the far right-hand column. Thus, for test conditions we expect heat transfer coefficients to vary from 25 to 40 w/m$^2$K.

**Table 2-2. Comparison of correlations for test conditions**

| | C | n(Re) | n(Pr) | NuFilm | h |
|---|---|---|---|---|---|
| Belov | 0.76 | 0.50 | 0.40 | 9.04 | 39.54 |
| Sogin | 0.20 | 0.67 | 0.00 | 6.37 | 27.88 |
| Hadad | 0.81 | 0.50 | 0.33 | 18.36 | 34.73 |
| Kang and Sparrow | 0.20 | 0.67 | 0.33 | 5.79 | 25.34 |

Testing results deemed to be valid were the second and third of the three tests conducted on September 30, 2013. These tests were conducted under slightly differing but largely similar conditions. Figures 2-15 through 2-20 below show the measured heat transfer coefficient results derived from the thermocouple data at three positions on the target; the stagnation point, front corner and mid-point on the side plotted as a function of time for the two tests.
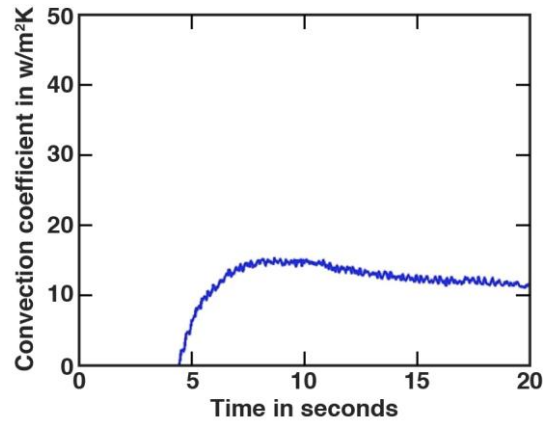
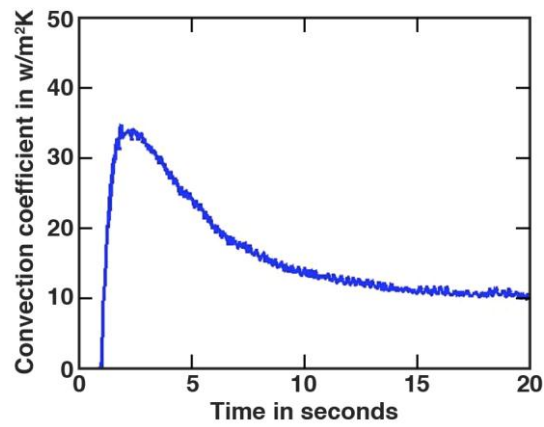*Figure 2-15. Measured convection coefficient at the stagnation point for the second test of Sept. 30, 2013*



*Figure 2-16. Measured convection coefficient at the front corner for the second test of Sept. 30, 2013*
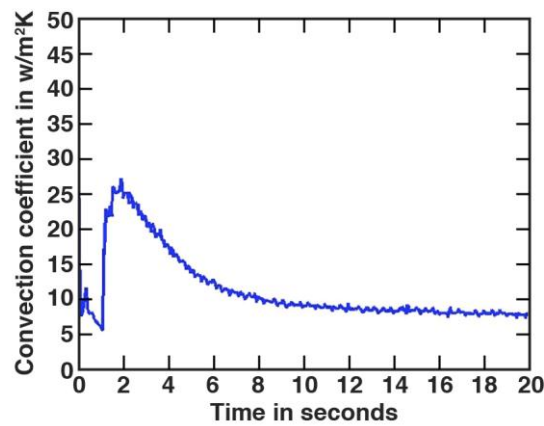


*Figure 2-17. Measured convection coefficient at the target side for the second test of Sept. 30, 2013*
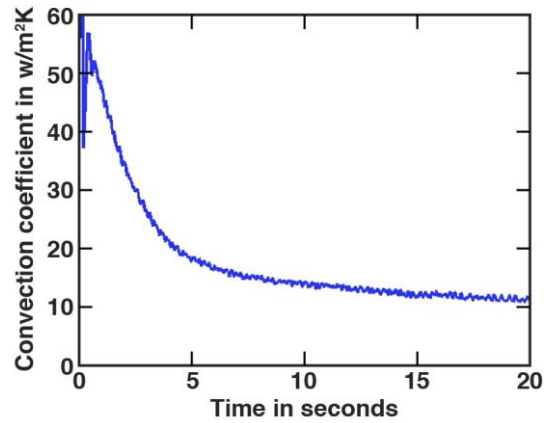
*Figure 2-18. Measured convection coefficient at the stagnation point for the third test of Sept. 30, 2013*
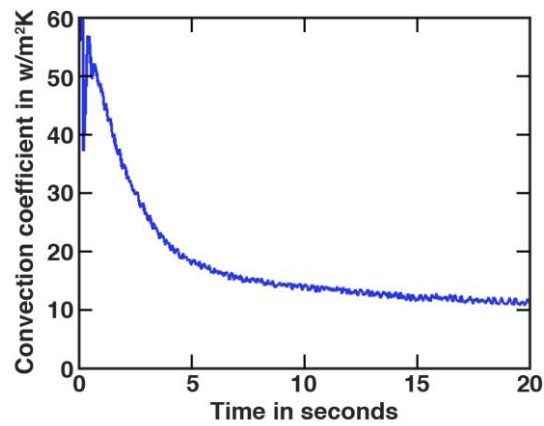


*Figure 2-19. Measured convection coefficient at the front corner for the third test of Sept. 30, 2013*
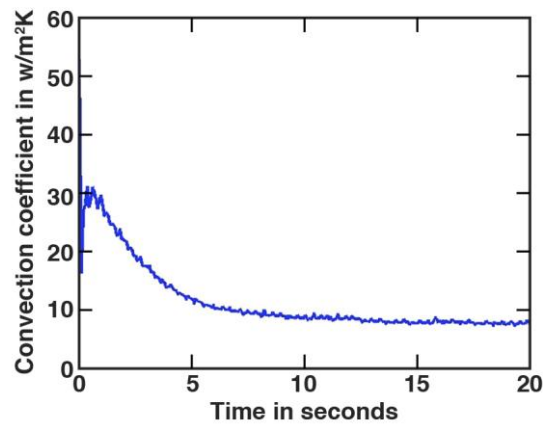


*Figure 2-20. Measured convection coefficient at the target side for the third test of Sept. 30, 2013*

For the plots of the second test, the first few data points plotted are actually pre-test data. Further, for all the plots the first few data points show very high scatter and should be considered unreliable. However the majority of the data over the first couple testing seconds is very good data and the results are consistent with both CFD modeling and the correlations described above. We expect that after two

19

to four seconds of testing local conductive effects to TC bead wires and the target shell support structure are becoming more significant relative to the thermal inertia effects quantified in the transient heat transfer equation given above. For both the second and third tests the dependence of the test results on thermocouple location is mostly as anticipated from the CFD (as shown in Figure 2-1). There is a high convection coefficient at the stagnation point. A significantly higher convection coefficient is observed at the corner point, here somewhat moderated from that shown in Figure 2-1 by the presence of local conductive effects. Lastly a lower convection coefficient is observed down the cylindrical side of the target, again as shown in Figure 2-1.

### 2.3 Conclusions

The magnitude of these heat transfer coefficients is largely consistent between the analysis and the test. The test results shown here validate the target flow and external heat transfer modeling performed in support of LIFE target design. Further work can be conducted to measure the heat transfer coefficient for target designs incorporating a recessed front end which can be used to reduce the heat transfer coefficient to the LEH window and/or the reduced thermal effects of a using a sacrificial layer on the LEH window.  Both options are discussed in Reference 1-6.

### 2.4 References

[2-1] Belov, I.A. and Terpigor'ev, V.S., Inzhenerno-Fizicheskii Zhurnal, **17.6**, 1106-109 (1969).

[2-2] Sogin, H. H. "A Summary of Experiments on Local Heat Transfer from the Rear of Bluff Obstacles to a Low Speed Airstream." *Transactions of the ASME: Journal of Heat Transfer* 86 (1964): 200-202.

[2-3] Hadad, Yaser, Khosrow Jafarpur. (2008, August). "Laminar Forced Convection Heat Transfer from Isothermal Bodies with Unit Aspect Ratio."  Paper presented at the 6th IASME/WSEAS International Conference on Heat Transfer, Thermal Engineering, and Environment, Rhodes, Greece.

[2-4] Kang, S. S., E. M. Sparrow. "Heat Transfer from an Open- or Closed- Bore Cylinder Situated Longitudinal to a Freestream." *Transactions of the ASME: Journal of Heat Transfer* 109 (1987): 314-320.

[2-5] Na, T.Y, and Pop, I, "Flow and heat transfer over a longitudinal circular cylinder moving in parallel or reversely to a free stream," Acta Mechanica 118 (1996): 185-195.

### 3.0 Internal heat transfer studies

The targets are shot downward into the fusion chamber in the LIFE design.  The leading LEH window is subjected to the highest heat flux due to the convective heat transfer from the chamber gases.  The hot LEH window generates convective currents in the helium gas internal to the target.  The objective of the internal heat transfer test was to investigate the convection currents induced by the heated leading LEH window and to note the temperature and pressure increases in the two helium chambers aft of the LEH window resulting from these currents.  The configuration for the experiment is shown in Figure 2-1.  A half-target was used for ease of measurement and because the leading half of the target becomes considerably hotter in the fusion chamber than the aft half and thus it is more important to study the leading half of the target.  The test LEH window consisted of a rapid heater that could reach about 250-

450K (starting temperature 77K) in 50-120 ms emulating the target flight LEH window which is expected to reach 1300 K in about 24 ms. The test "hohlraum" was a stainless steel block that emulated the thermal mass of the lead hohlraum.  The IR window consisted of a 1 um thick polyimide membrane which supported a 5mm OD by 0.2 mm thick test "P2 shield", similar to the nominal design.  The "capsule" position was replaced by a very low thermal mass, fast response time temperature sensor such that the few degree expected temperature rise could be measured. The helium density was about 1 mg/cc, about 1 atm pressure at 77K, similar to densities in the fusion targets at 18K. Tests were conducted with both a sealed IR shield and with some by-pass flow around the IR shield.

### 3.1 Test set-up

The experiment was designed to provide experimental data (pressure and temperature) for validating a simulation of a cryogenically-cooled LIFE hohlraum subjected to a brief (~24 ms) high thermal load on the thin LEH membrane at one end of the target.  As shown in Figure 3-1, the internal geometry of the apparatus approximated the leading bottom half of a LIFE target.  The stainless steel housing was comp0rised of two pieces, creating an upper and lower chamber.  Pressure sensors were mounted into each chamber.  The chambers were separated by a 1-micron-thick polyimide membrane.  The membrane was supported by and glued to two 0.125-mm-thick sheets of polyimide. A lead disc was attached to the center of the polyimide membrane.  This membrane mimicked the IR shield with attached lead P2 shield in a fusion target.  The lead disc was instrumented with two thermocouples. Silicon wafers with silicon-nitride membranes with dual thin-film-platinum serpentine traces patterned on the membranes were located on the top and bottom of the housing.  One of the traces on the bottom membranes was used as a heater to mimic a fusion target LEH window heated by the hot gases of a fusion chamber; the other trace was used to measure the temperature.  The traces on a second membrane became a sensor used to measure the temperature at the position where a capsule in a fusion target would be mounted. The desired test environment was a helium atmosphere at 77K and atmospheric pressure to mimic the effect of the convection currents in a helium filled target.  A mechanism with indium seals was used seal the top and bottom chambers once the test conditions of the internal helium atmosphere were achieved.
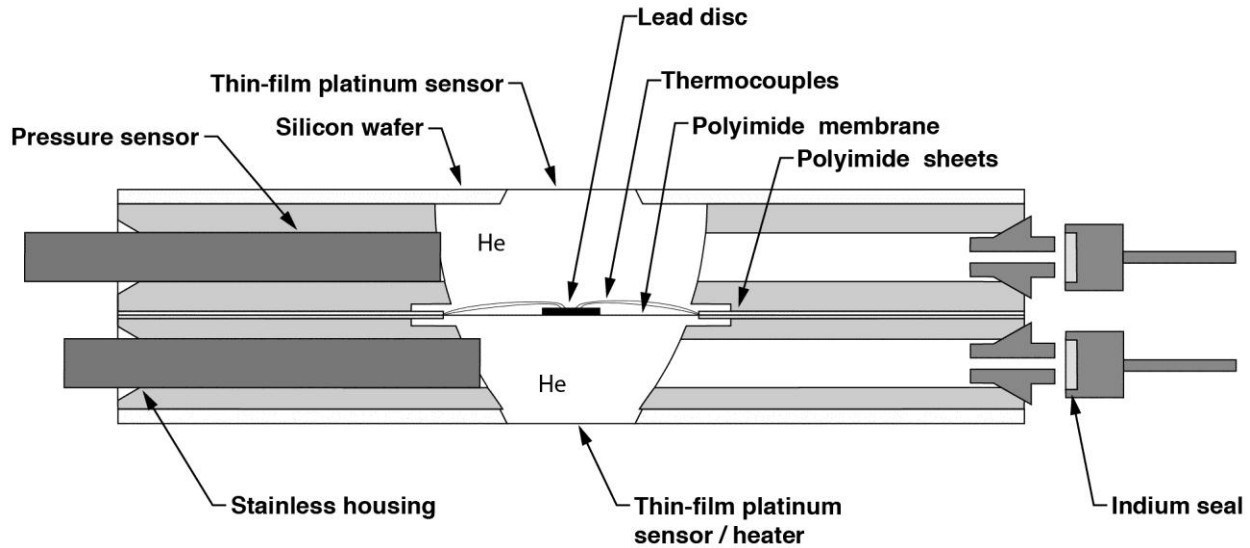
*Figure 3-1.   Cross-sectional schematic view of the experiment.*

### 3.2 Fabrication of the apparatus

*Hohlraum pieces*

The stainless hohlraum pieces (AAA13-501013-AA and AAA13-501013-AA) were fabricated at LLNL. Following the machining, the outer surfaces (sides without the counterbore) were lapped flat and smooth so that a seal could be achieved against the silicon wafers without adhesive.

*Chamber seals*

The indium seal design was developed via trial and error; the final shapes are as shown in Figure 3-1 above.  The stainless inserts were bonded to the housing using Hardman double bubble epoxy.  A fixture was used to ensure that both inserts protruded the same distance from the housing. The indium seats were punched from 0.25mm-thick sheet and pressed into the stainless holders.  The indium seats were replaced each time the apparatus was brought up to atmosphere after each use.

*Seal mechanism*

A manually operated, rotary to linear motion mechanism was designed to close the seals once the apparatus had achieved the desired environment, 1 atmosphere of helium at 77K (Figure 3-2).   Rotation of the cam causes the indium seals to be pressed into the mating pieces on the stainless housing.
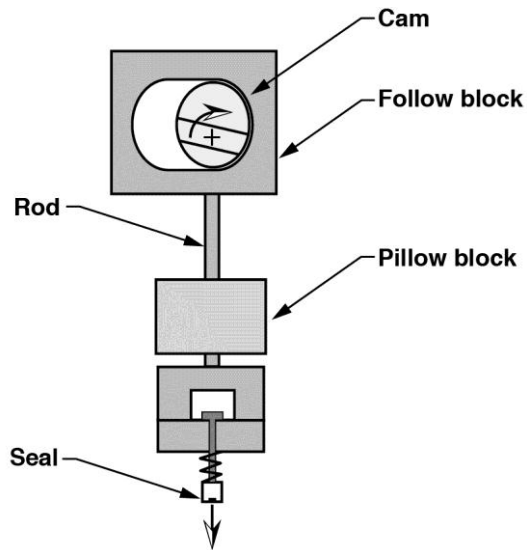
*Figure 3-2. Seal Mechanism. Rotation of the cam about its off-center axis causes the follow block and rod to move downward as shown.*
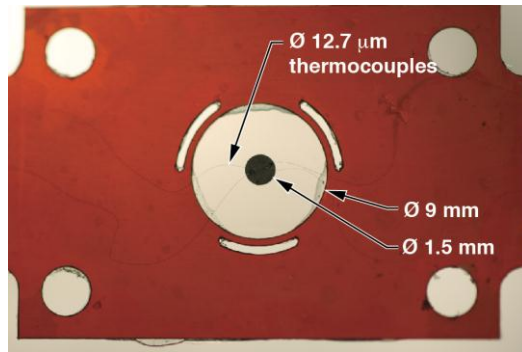
*Membrane assembly*

The membrane assembly consists of a thin polyimide membrane supported by thicker sheets of polyimide on both sides. A 5-mm-dia. lead disc instrumented with two thermocouples was bonded in the center.

The lead discs were instrumented at LLNL. A sharp knife was used to lift up "flaps" of material from the surface. Two 12.7-um-dia, type E (chromel – constantan), pre-beaded bare wire thermocouples were inserted into the flaps and the flaps pressed down to hold the beads in place.

The outer sheets of the membrane assembly were laser cut from 0.125-mm-thick Kapton HN at LLNL. Two types were fabricated – one having three slots around the center hole (bypass configuration) and one without (solid configuration). The bypass configuration in shown in Figure 3-3. The Kapton was prepared for adhesive bonding by lightly abrading the surfaces with 12 micron alumina film. The prepared frames were cleaned and sent to Luxel[1] who fabricated and bonded the 1-micron-thick, Upilex-type polyimide to one side using epoxy. Luxel also bonded the lead disc / thermocouple assembly to the center of the membrane. At LLNL, the second sheet of Kapton was bonded to the 1-micron-thick membrane using Epon 828 / Versamid 125 epoxy, sandwiching the thermocouple wires between the two Kapton layers.

---

[1] Luxel Corporation, Friday Harbor, WA

*Figure 3-3.  Bypass membrane assembly.  The lead disc is glued to the 1-micron-thick polyimide membrane.  Thermocouple wires are bonded between the sheets of Kapton.*

The small-diameter thermocouple wires were spot-welded to thermocouple alloy tabs (Figure 3-6). Larger diameter (127 um) thermocouple wire was welded to the tabs and routed to through the patch panel on the underside of the apparatus to the type E thermocouple feed-throughs (Figure 3-5).

Because the assembled membrane assemblies were not sufficiently flat to achieve a good seal to the hohlraum pieces, rings of thin, rubber double-stick adhesive were used to form the seal.

*Platinum sensor/heater*

The platinum sensor/heater consisted of a set of two thin film platinum strips that are each 100 $\mu$m wide and 200 nm thick, and arranged in a serpentine pattern (Fig. 3-4). Each end of the platinum serpentine strips was connected to a large pad, and electrical wiring can be soldered onto the pads to make connection with the sensor/heater. Each platinum serpentine strip had an electrical resistance of around 220 $\Omega$ at room temperature.

The thin-film sensor/heaters were fabricated on 500 nm of silicon nitride thin film on 0.5mm-thick silicon wafers by photolithography.  A KOH etch process was used to open a hole through the silicon underneath the sensor/heater, such that the sensor/heater were suspended on a 5 mm x 5 mm silicon nitride membrane.
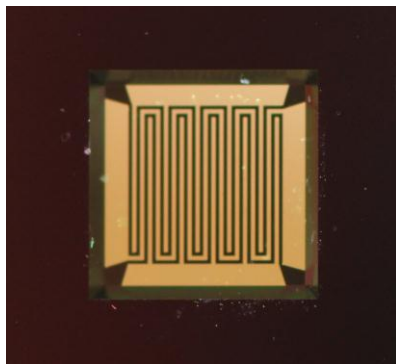


*Figure 3-4.  Photograph of a thin film platinum sensor / heater as would be viewed from inside the hohlraum.*
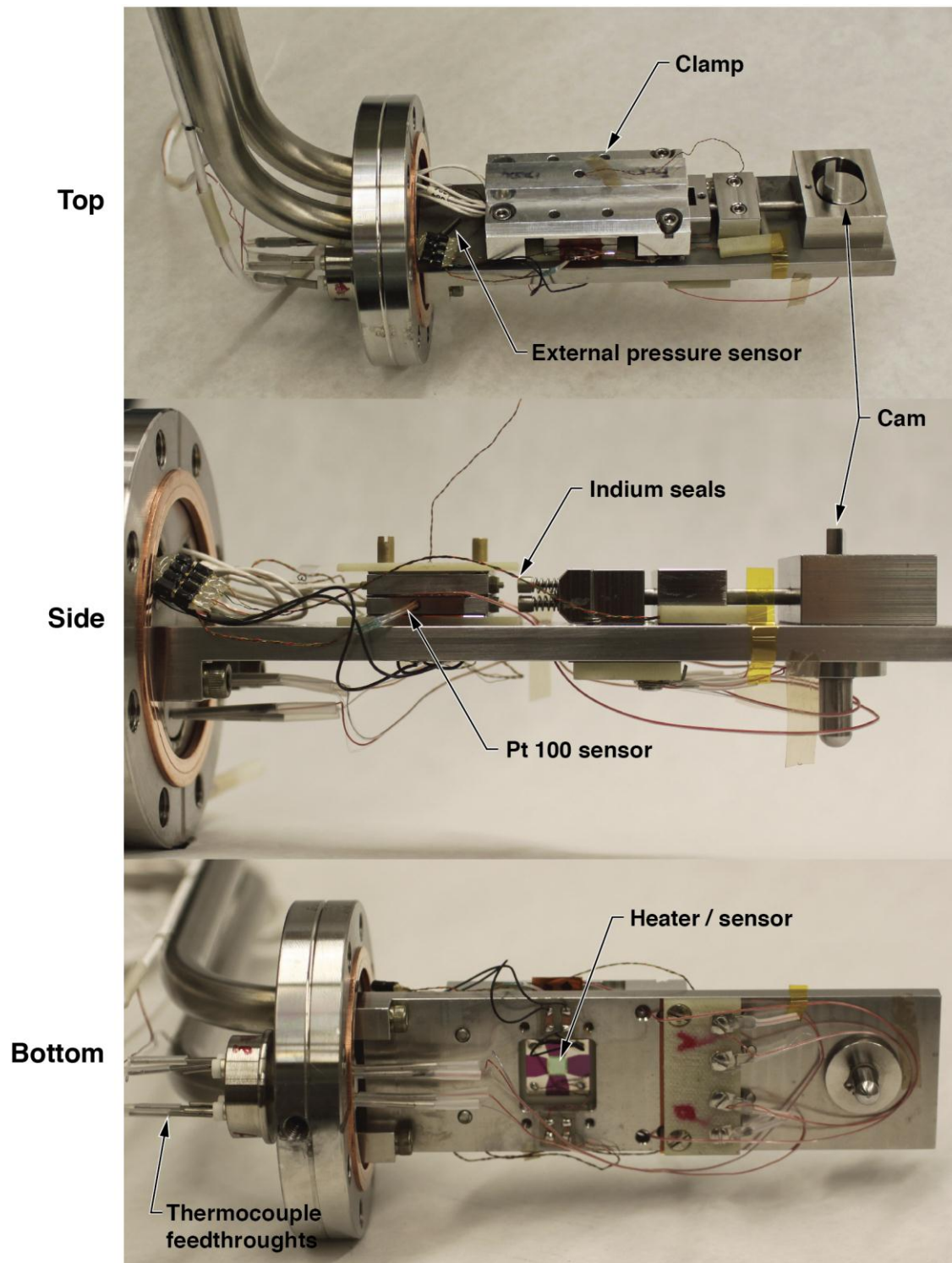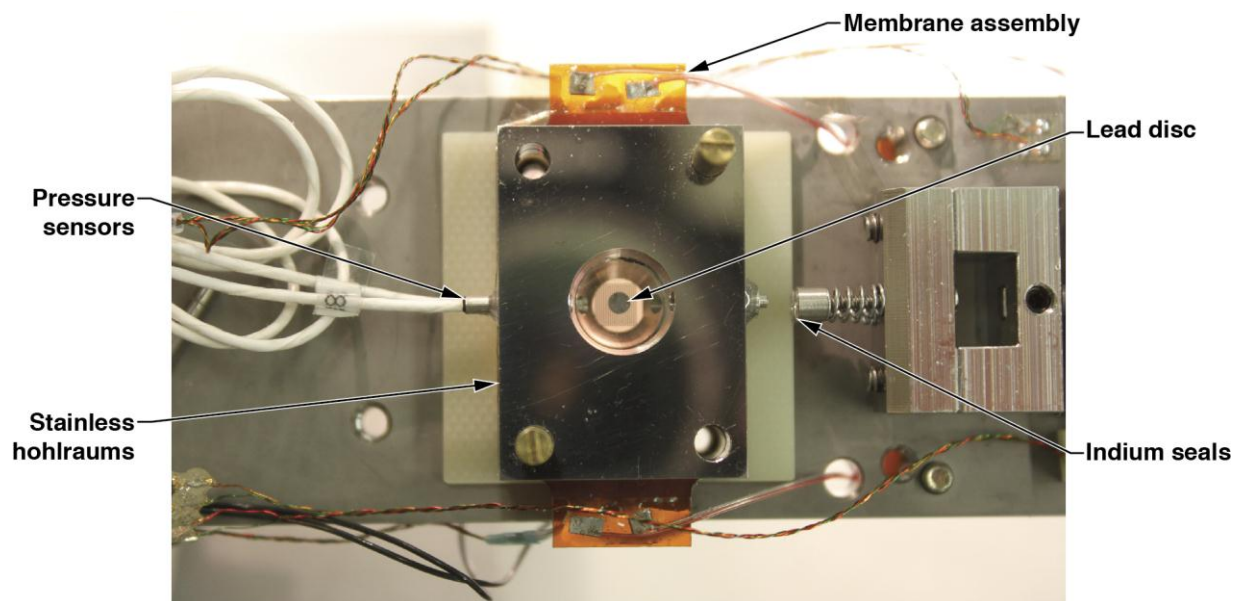
*Figure 3-5.  Three views of the assembled apparatus.*

*Figure 3-6.  The assembled apparatus with the clamp and top silicon piece removed.*

*Housing*

The experiment was mounted inside a sealed can submerged in a dewar of LN.  As shown in Figure 3-7, the instrumentation feed-throughs and cam actuator were mounted in tubes long enough to keep the seals close to room temperature.
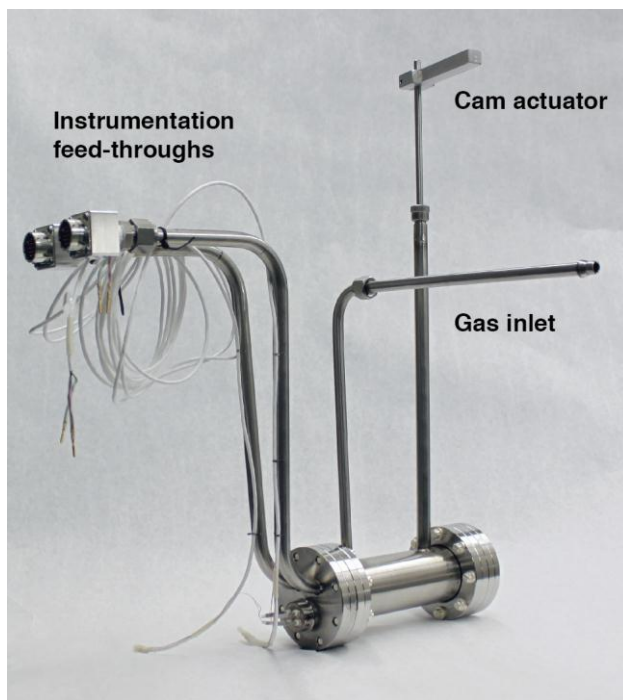


*Figure 3-7.  Outer housing.  The experiment is contained in a can so that it can be submerged in a dewar of LN.  The feed-throughs are on tubes that extend outside of the dewar.*

### 3.3 Sensors and instrumentation

*Pressure Sensors*

The experiment was instrumented with three Kulite pressure sensors. Two were mounted in the stainless hohlraum chambers as shown in Figures 3-1 and 3-5 using Hardman epoxy.  A third sensor was installed in the area immediately outside the hohlraum (Figure 3-5).  The pressure sensor specifications and instrumentation settings are shown in Table 3-1.  Micromeasurements 2210 signal conditioners with an excitation of 10V were used.  Because the zero balance of the sensors was not particularly precise, the bridge output was balanced at ambient atmosphere and measurements were made relative to ambient instead of absolute pressure.  The sensors also exhibited a significant zero shift with temperature.  The zero shift was subtracted once the system reached steady state at 77K.

**Table 3-1.  Kulite Pressure Sensor Data**

| Sensor location | Top hohlraum (away from heater) | Bottom hohlraum (near heater) | Inside can |
|---|---|---|---|
| **Sensor model** | CCQ-062-7BARA | CCQ-062-7BARA | CCQ-062-1.7BARA |
| **Range (Bar)** | 7 | 7 | 1.7 |
| **S/N** | 384 | 383 | 540 |
| **Excitation used** | 10.002 V | 10.040V | 10.040V |
| **Sensitivity** | 14.214 mV/BARA | 14.237 mV/BARA | 54.841 mV/BARA |
| **Zero offset (typ.)** | ± 352 mB | ± 351 mB | ± 91 mB |
| **Atmospheric pressure (as-measured, unbal-anced output)** | 880mB | 924 mB | 995 mB |
| **Thermal zero shift (typ.) RT to 77K** | ± 280 mB | ± 280 mB | ± 68mB |
| **Nat. Freq. (typ.)** | 380 kHz | 380 kHz | 240 kHz |
| **Amplifier gain used** | 100 | 100 | 100 |
| **Nicolet scale used** | 704.6 mB/V | 700.7 mB/V | 184.9 mB/V |

*Lakeshore temperature sensors*

Two Lakeshore[2] sensors were used ;  a wire-wound platinum (PT-111-2S) sensor placed into a recess in the lower stainless hohlraum, and a Cernox bare chip sensor (CX-1070-BC-HT-4L) mounted on a G-10 rod.  The Cernox sensor was originally intended to be placed inside the hohlraum to calibrate the thermocouples in-situ.  When the seals were re-designed with indium seats there was not room to install it.  Instead, it remained inside the can but outside the hohlraum.  The temperature data collected during the gradual warm-up of the experiment showed that the PT-111 sensor was a closer match to the thermocouples and thin film Pt sensors.  Therefore the PT111 sensor was used to derive the calibration scaling for both the thermocouples and thin film Pt sensors.

---

[2] Lakehore Cryotronics, Westerville, OH

The PT-111-2S was ordered with 3-point SoftCal data.  The output of both sensors was monitored with a Lakeshore 218 temperature monitor.

*Thin-film platinum sensor/heaters*

The thin film Pt sensors were connected with four leads:  two for the constant current source, and two for the voltage measurement.  A constant current excitation of 100 uA was provided by Lakeshore 120 current sources.  The output voltages were amplified by 100 using Stanford Research Systems SR560 low-noise amplifiers.

The sensors were calibrated by comparing the output to the Pt-111 sensor output during the gradual warm-up of the apparatus.  The response of the upper sensor, which was not exposed to temperatures above 300K, remained repeatable throughout our series of experiments (Figure 3-8).   The lower sensor showed a permanent change in resistance following exposure to elevated temperature.  In order to ensure that an accurate calibration was available for every test, a warm-up experiment was performed following experiments in which a resistance change was noted.
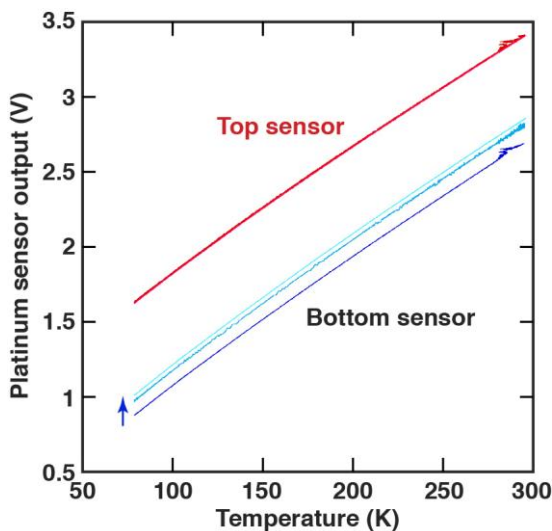


*Figure 3- 8.  Thin-film platinum sensor output as a function of temperature, measured after several series of experiments.  The bottom sensor was exposed to elevated temperature during the experiments, causing an increase in resistance and an upward shift in the calibration curve.*

Because calibration data was not available for temperatures exceeding room temperature, the linear portion of the calibration curve (above 175K) was extrapolated (Figure 3-9).  A third degree polynomial accurately represents the measured data from 77 to 300K.
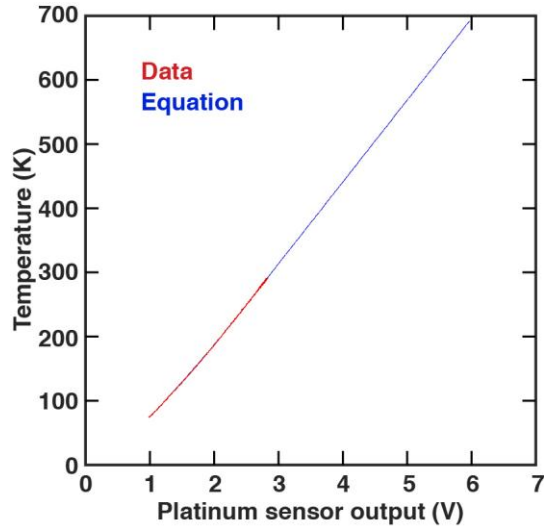
*Figure 3-9.  A third degree polynomial fit was used to calculate temperature from the platinum sensor output over the range of 77K to 300K.   Temperatures above 300K were estimated by extrapolating a linear fit to the data above 175K.*

*Thermocouples*

The thermocouple cold junction was formed where thermocouple wire welded to the outside thermocouple feed-throughs was connected to the copper cable.  This junction was submerged in the LN during the tests.  The output voltages were amplified by a gain of 200 using SRS560 amplifiers.

The thermocouple output voltage was calibrated against the PT111 sensor temperature during warm-up of the apparatus.  Since the measured temperature excursions of the thermocouples were small (less than 10K), a linear fit was used (Figure 3-10).  The fit as calculated is within 4% of the NIST table values.
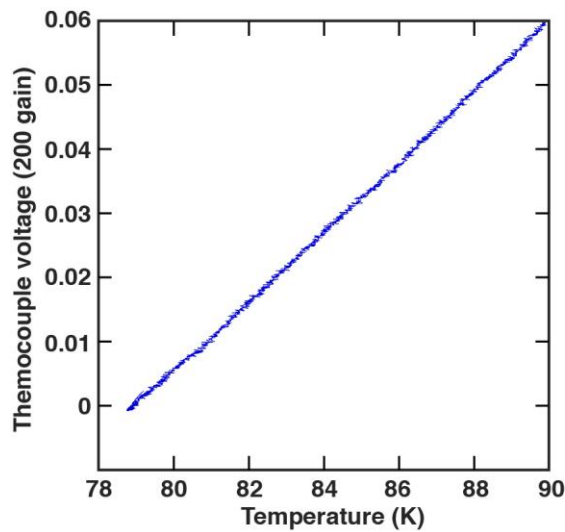


*Figure 3-10.  Thermocouple output vs. temperature.  A linear fit was used over the range of 78-90K.*

3.*4 Experimental Procedure*

The apparatus was assembled and lowered into the dewar with the internal seals in the "open" position. The manifold connecting the vacuum pump and helium source was connected. The pressure sensors were then zero balanced at ambient pressure. The helium regulator was set to apply pressure just slightly above atmosphere.  The system was then evacuated and back-filled with helium several times. After the final fill the helium valve was left open to add additional gas as needed as the system was cooled.

Liquid nitrogen was poured into the dewar until the can of the apparatus was completely submerged.  A foam lid was used to retard the loss of liquid nitorgen.  The temperature inside the can was monitored to indicate when the apparatus had fully cooled.  The external lever was then used to seal the hohlraum chambers in preparation for testing.  A photograph of the cooled apparatus is shown in Figure 3-11.

Tests were conducted by applying a 60 – 250 ms voltage pulse to the heater and recording the output of the pressure and temperature sensors.  The voltage pulses were generated using an HP 33120A function generator.  A Trek 2100HF Piezo Driver was used to increase the current in order to drive the heater.  A summary of the tests conducted is shown in Table 3-2.
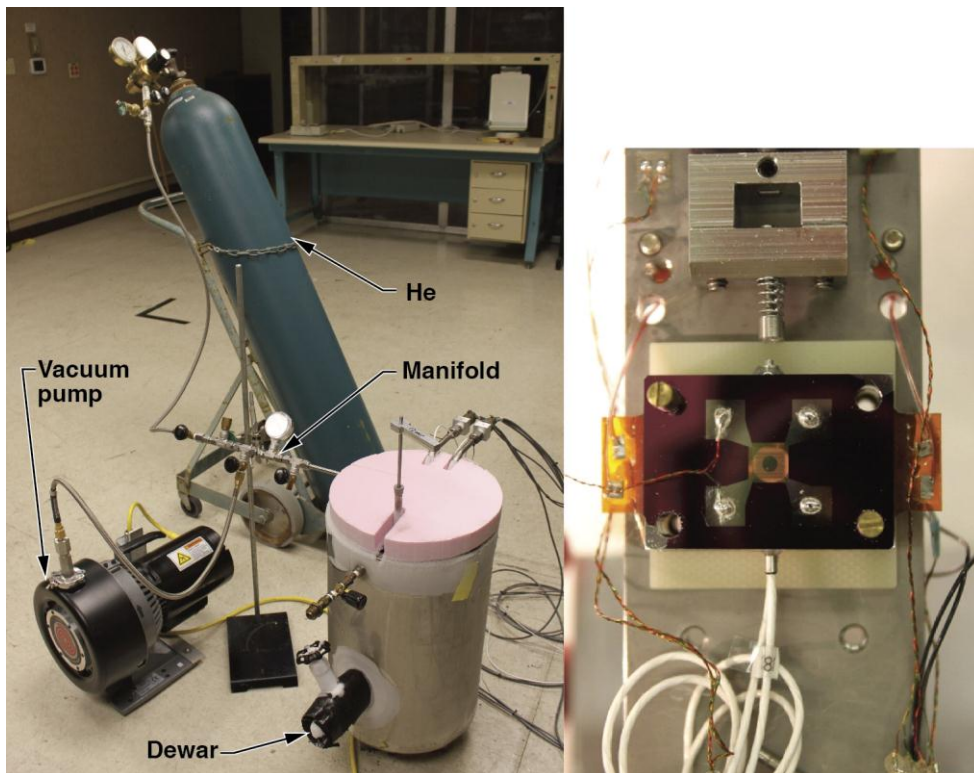


*Figure 3-11.  Apparatus is installed in the dewar and ready for test.*

### 3.5 Analysis and results

The analytical model for the internal heat transfer test with helium gas "bypass" is shown in Figure 3-12 below. Models with "bypass" mean that flow of the internal helium gas was permitted between the target helium compartments. Key parts of this half symmetry model are the steel shells which contain the helium gas, the central assembly membrane and the P2 shield.
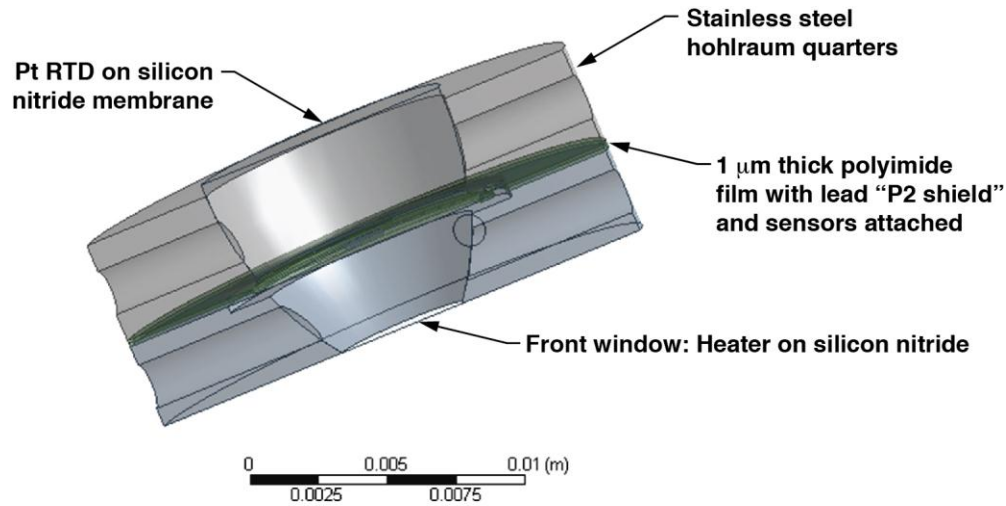


*Figure 3-12. Finite element model of internal heat transfer test assembly with helium "bypass"*

The central membrane of this assembly is shown in Figure 3-13 below. The small central yellow disk in this figure is the P2 shield. The darker gray outer portion of this item is the membrane area that is sandwiched between the steel shells. The lighter gray central circular portion of this item is the IR shield portion of this item. The arcing $60^\circ$ and $30^\circ$ cutouts of this item are the "bypass" features, the cutouts for helium to move freely between the two sides of the IR shield so that frontal helium pressure does not cause the thin LEH and IR shield membranes to rupture.
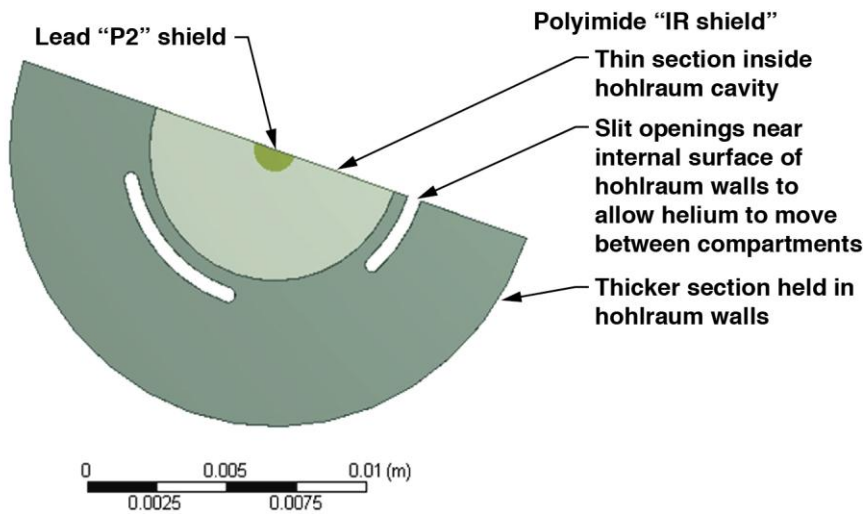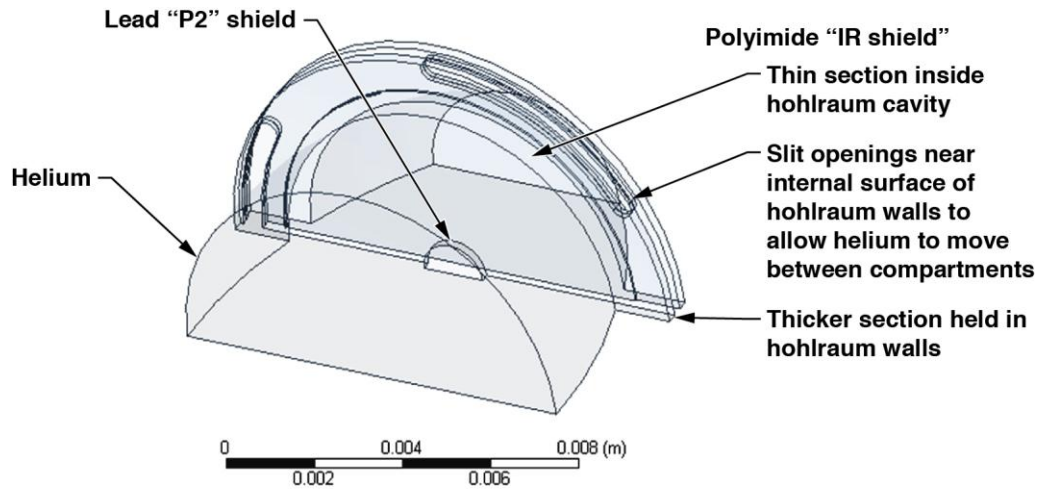


*Figure 3-13. Central membrane of test with "bypass" assembly*

The portion of the model which is the helium gas fill is shown in Figure 3-14 below. This is a single connected helium zone with boundaries on the P2 shield, the upper and lower steel shells and the central membrane.



*Figure 3-14. Helium zone within model of test assembly with helium "bypass"*

The semicircular face of the helium zone closest to the viewer in this picture is actually the "top" face of the assembly in the "as tested" configuration and is the equivalent of the cold capsule-support membrane surface in the target design concept. The test is meant to confirm the prior modeling regarding heat flow to this area and thus to confirm or refute the assertion that the DT ice heating in the target design is less than the specified maximum of 0.1 K. The semicircular face of the helium zone furthest from the viewer in the view of Figure 3-14 is the surface of the helium in intimate contact with the front LEH window membrane, where the platinum heater applies a precise thermal pulse qualitatively but not quantitatively similar to the heating of hot xenon during flight through the target chamber.

This model was created using ANSYS workbench and its geometry and meshing tools. Thermal and fluid calculations were done using the CFX option of ANSYS. A few details of the model are given in Table 3- 3 below.

**Table 3-3. Some modeling parameters for the internal heat transfer test with "bypass" assembly**

| Simulation information | |
|---|---|
| Nodes | 471153 |
| Time step size | 0.00002 sec. |
| Steel external convection coefficient | 5 w/m$^2$K |
| Assembly external fluid temperature | 77K |
| Cold top convection coefficient | 5 w/m$^2$K |

The choice of external convection coefficients has not been rigorous, or checked. It is expected that these parameters have weak influence on the results since the thermal inertia of the steel shells is large compared to the product of the test time and the other heat input terms of the test. Material properties used in the simulations discussed here are given in Table 3-4 below.

**Table 3-4. Material properties used in simulations**

| Material | Density | Specific heat | Thermal conductivity | Viscosity |
|---|---|---|---|---|
| (-) | (kg/m3) | (J/kgK) | (w/mK) | (Pa-s) |
| helium | perfect gas | 5194 | functional | 9.66E-06 |
| lead | 11360 | 113.8 | 40 | - |
| steel | 7855 | 434 | 10 | - |
| polyimide | 1420 | 1090 | 0.12 | - |

The constant values shown for most of the entries in the table were selected based on the range of test temperatures expected, i.e. 77K for steel, 77K and slightly warmer for lead, and 77 to 650K for polyimide. The specific heat of helium is very insensitive to temperature over the expected range for the tests. The functional form used for the thermal conductivity of helium is a simple linear fit: k = (4.3263e-5*T+.030264) w/mK. A similar or more complex fit to the viscosity of helium may be a useful improvement. Lastly, the actual specific heat of polyimide used in the model is reduced from the value shown in Table 3-4 by the ratio of the actual test membrane thickness divided by the model membrane thickness. The model membrane thickness is larger to facilitate meshing and computation. To compensate, the specific heat is reduced so that membrane thermal inertia is correctly modeled.

The face of the helium zone adjacent to the platinum heater (and/or the LEH) has been given a range of temperature boundary conditions depending on the joule heating pulse applied to the heater in particular tests.  These boundary conditions take the form of fourth and fifth order polynomial curve fits to the measured heater membrane temperatures.  Figure 3-15 below compares measurements and curve fit for one such test. The fit is good and use of the fit in the modeling simplifies the simulation work. It eliminates both the need to model the "LEH window" in the test and to resolve the interaction between the solid membrane and the helium beside it. Table 3-5 below lists the curve fits for all five of the "without bypass" tests for the test configuration. "Without bypass" means that there is no helium flow between internal compartments.



The equation shown on the figure: $y = 1.3383E{+}06x^5 - 9.8175E{+}05x^4 + 2.7403E{+}05x^3 - 3.6388E{+}04x^2 + 2.3372E{+}03x + 8.4255E{+}01$
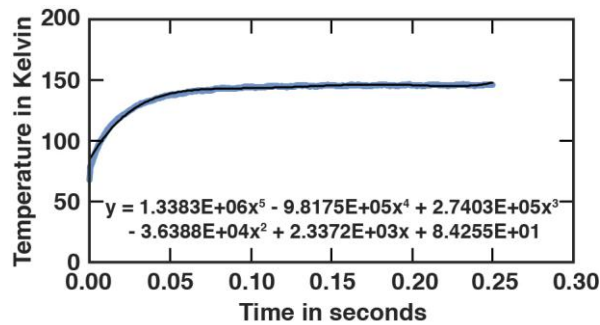
*Figure 3-15. Comparison of platinum heater measured temperature history and curve fit used to drive thermal simulation of assembly heating transient*

**Table 3-5. Curve fitting constants for the LEH membrane heater deployed on the "without bypass" (solid membrane) tests**

| Test | Peak temperature | C5 | C4 | C3 | C2 | C1 | C0 |
|------|------------------|------|------|------|------|------|------|
| (-) | (K) | (K/s5) | (K/s4) | (K/s3) | (K/s2) | (K/s) | (K) |
| SM1 | 146 | 1.33830E+06 | -9.81750E+05 | 2.74030E+05 | -3.63880E+04 | 2.33720E+03 | 8.42550E+01 |
| SM2 | 256 | 1.10590E+08 | -4.10040E+07 | 5.79530E+06 | -3.91020E+05 | 1.28450E+04 | 8.13760E+01 |
| SM3 | 460 | 7.60380E+09 | -1.41880E+09 | 1.01220E+08 | -3.45920E+06 | 5.77760E+04 | 5.72780E+01 |
| SM4 | 613 | 1.70190E+10 | -3.09350E+09 | 2.11910E+08 | -6.77230E+06 | 1.00590E+05 | 4.06790E+01 |
| SM5 | 626 | 7.14140E+10 | -1.01080E+10 | 5.36490E+08 | -1.31300E+07 | 1.46550E+05 | -1.84390E+00 |

The model for the test without helium gas "bypass" is shown in Figure 3-16 below.
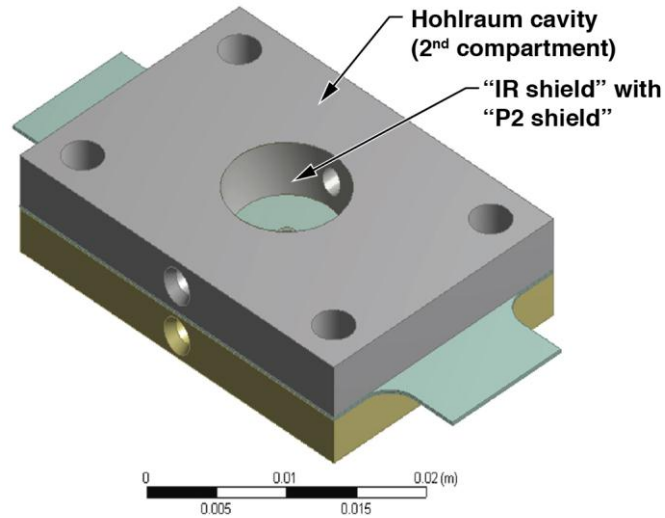
*Figure 3-16. Finite element model of test #1 assembly without helium "bypass" (no helium flow between compartments)*

In contrast to the "bypass" model this model assumes no symmetry. The steel shells sandwiching the central membrane (IR shield) are essentially the same as in the "bypass" model. Further details of this model are shown in Figures 3-17 through 3-19. Figure 3-17 shows the shape of the lower helium compartment (nearest the Pt heater) and Figure 3-18 shows the upper helium compartment. Figure 3-19 shows both helium compartments. These are the two separate fluid zones of the model, each of which interacts with the steel shells shown in Figure 3-16. Boundary conditions and model evaluation are similar to those applied to the "bypass" model.
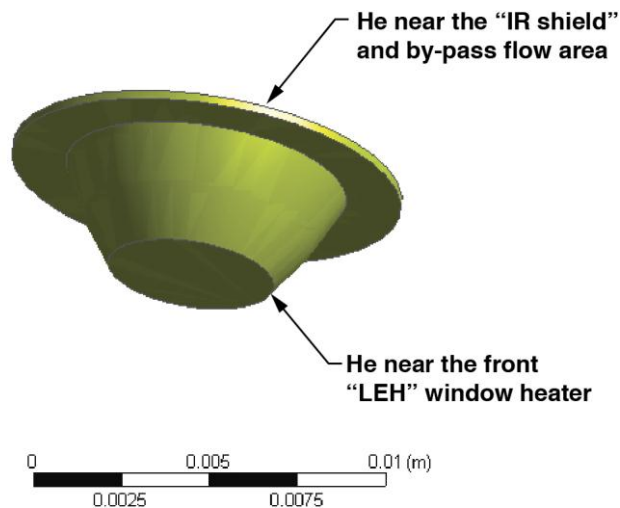


*Figure 3-17. Model of lower helium zone of internal heat transfer test (without "bypass")*
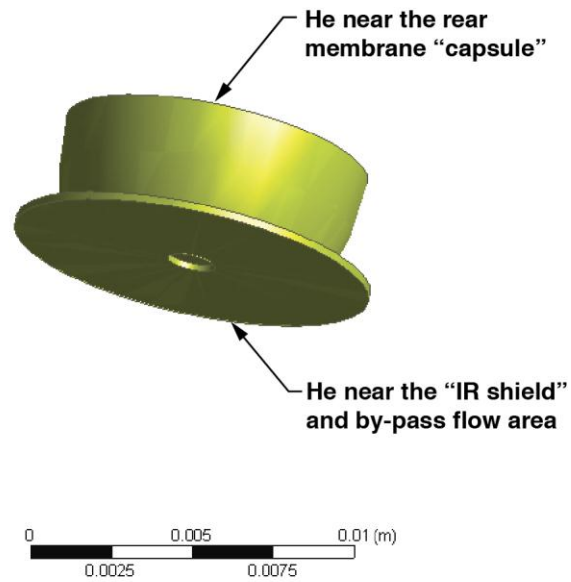
*Figure 3-18. Model of upper helium zone of internal heat transfer test (without "bypass")*
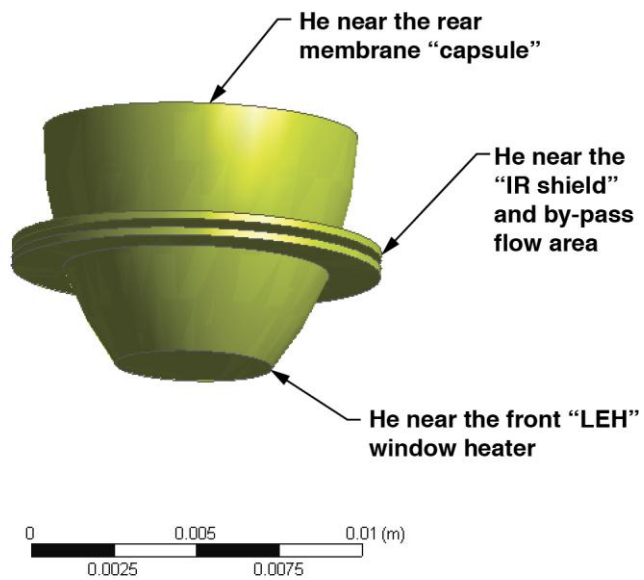


*Figure 3-19. Both helium zones of internal heat transfer test "without bypass"*

The "without bypass" model uses the same material property data and similar Pt heater histories as those given above for the "bypass" model.

### 3.5.1 Comparison of the test results with the model results

### 3.5.1.1. Comparison of test and data for internal heat transfer test with "bypass" (with helium flow between compartments)

Results for the "bypass" model with the LEH driven rapidly to 450K (corresponding to test BP3 performed on 8/27/2013) will be discussed here. The temperature transient for the maximum temperature on the LEH face is shown in Figure 3-20. The small oscillation in the maximum beyond 0.08 seconds is due to the use of a polynomial fit for this driving boundary condition and should not significantly degrade the results.
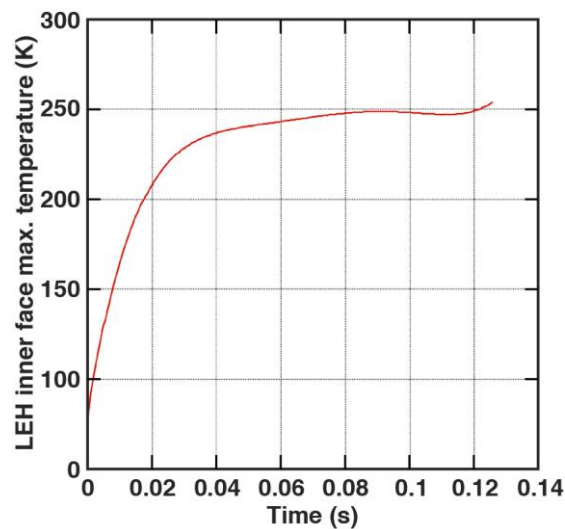


*Figure 3-20. Simulation transient maximum temperature on the LEH face from the "bypass" model*

Figure 3-21 shows the temperature profile on the central membrane (P2 shield) late in the simulation. The variation in temperature, due to the flow patterns developed around and through the bypass passages, is not large. The hot spots are from upwelling convection currents impinging upon the membrane.
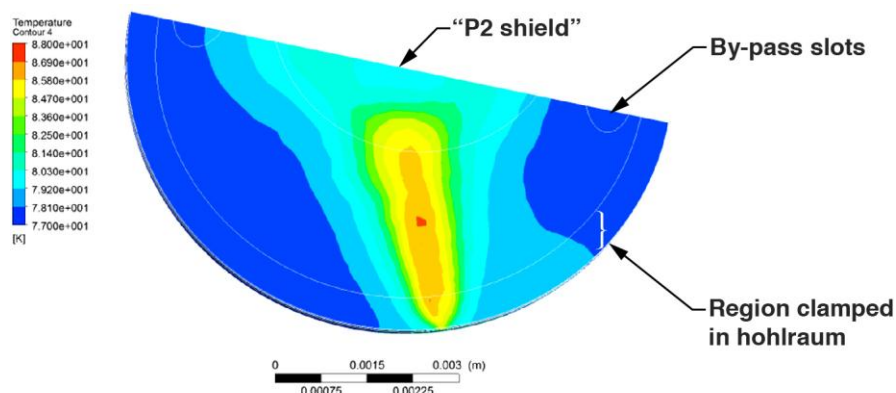
*Figure 3-21. Simulation result for temperature profile on central membrane of the "bypass" model.*

Figure 3-22 shows the transient of the average value of the absolute pressure in the helium charge in the model. This contrasts to the measured pressure of the charge shown in Figure 3-23. Given that pressure rise in testing is almost twice (~8 kPa vs. ~4 kPa) that of simulation this is not good agreement between simulation and test.
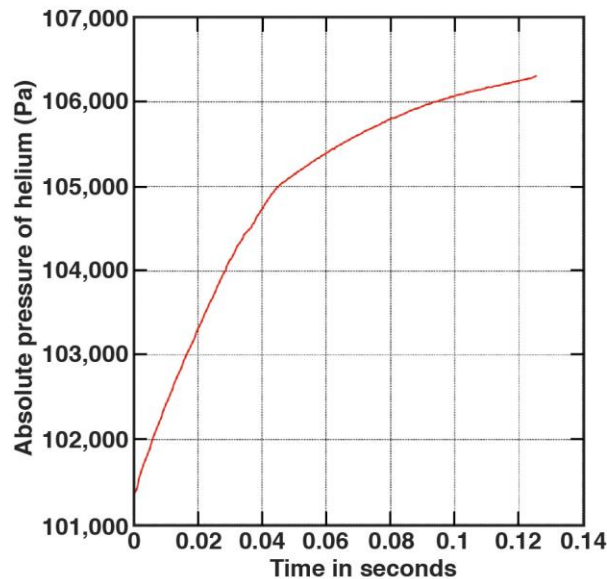


*Figure 3-22. Simulation transient of the average value of the absolute pressure in the helium charge of the "bypass" model*
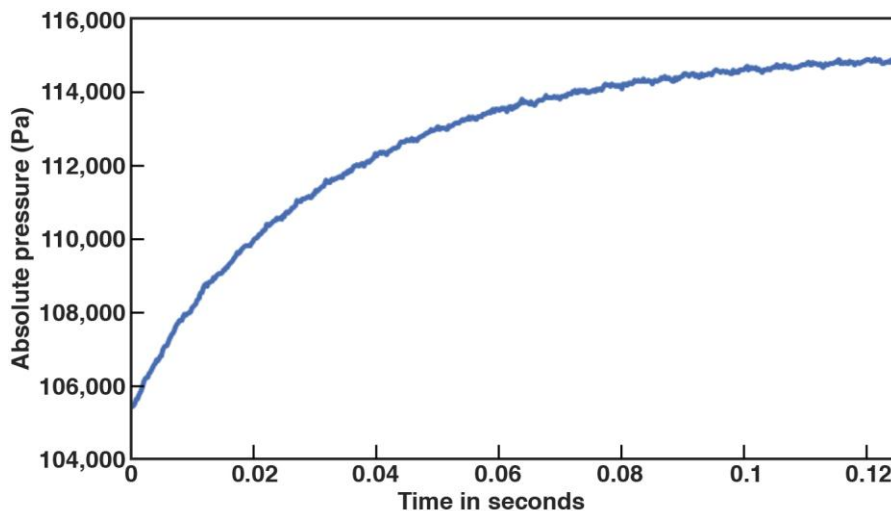


*Figure 3-23. Measured transient of the absolute pressure in the helium charge of the "bypass" test*

Figure 3-24 below gives the simulation transient for the average temperature of the P2 shield, which should be compared to the measured transient for the temperature sensor attached to the P2 shield shown in Figure 3-25. The simulation result, about a 0.6 K rise in temperature after about a 0.04 second lag period contrasts to about a 1.4 K rise in the measured (estimated on the sinusoidal time varying curve) which also has about a 0.4 second lag in response as well. Despite the similar lag times one would not describe this as good agreement between simulation and test.
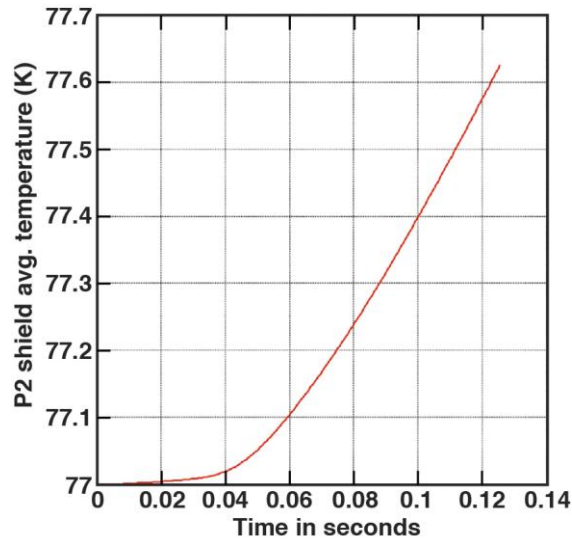


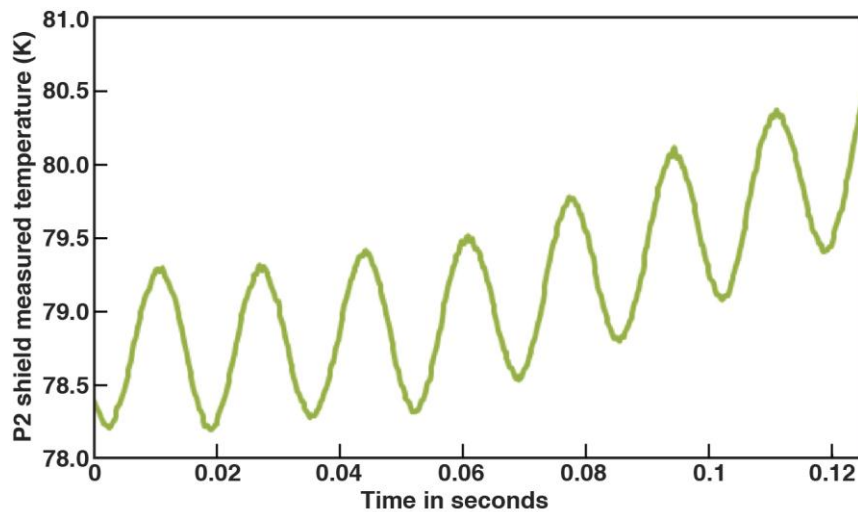*Figure 3-24. Simulation transient of the average temperature of the P2 shield of the "bypass" model*



*Figure 3-25. Measured transient of the sensor at the P2 shield of the "bypass" test*

Figure 3-26 shows the simulation transient maximum temperature on the top face of the "bypass" model, which compares to the measured transient response of the thermal sensor at the top membrane of the test where the target capsule would be located. The simulation result, with temperature rising until ~.042 seconds and then falling afterwards, seems in error.   If one considers only the first 0.04

seconds, the simulation has a 0.44 K temperature rise and over the same time period the test shows a 0.7 to 0.8 K temperature rise, about twice the simulated value.  Again, this is not good agreement.

The overall results for the "bypass" model indicate a discrepancy between the test results for pressures and temperatures and the predicted results of about a factor of 2.  More work would be required to determine the source of these discrepancies.
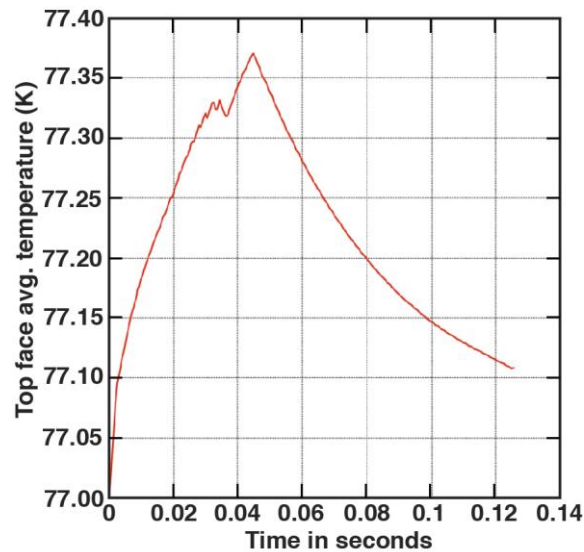


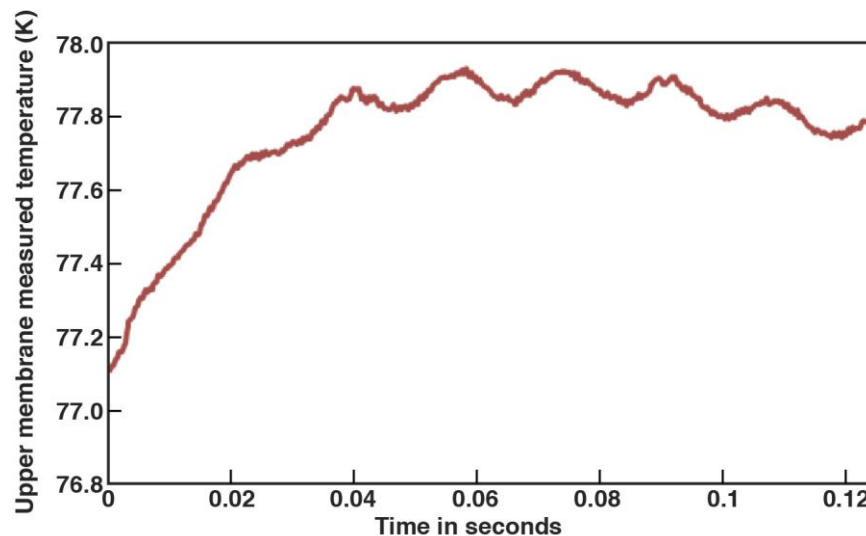*Figure 3-26. Simulation transient of the maximum temperature of the top face of the "bypass" model*



*Figure 3-27. Measured transient of the sensor at the top membrane of the "bypass" test*

### 3.5.1.2 Comparison of test and data for internal heat transfer test without "bypass" (no helium flow between compartments)

Results for the "without bypass" model with the LEH driven rapidly to 250K will be discussed here (corresponding to test SM3 performed on 9/14/2013. Figure 3-28 shows the transient average temperature for the LEH. The polynomial fit used to get this time history clearly fails after 0.045 seconds so only results to 0.05 will be shown and discussed here.
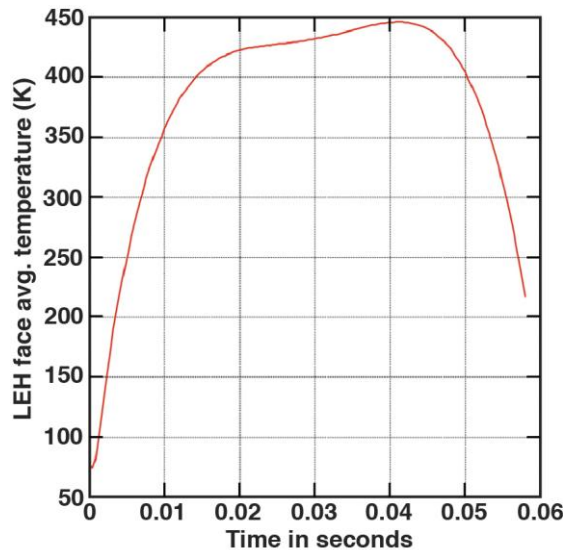


*Figure 3-28. Simulated transient average temperature on the LEH face from the "without bypass" model*

The simulated transient pressure history in the helium compartment adjacent the LEH is shown in Figure 3-29. This result contrasts to the measured transient histories in both helium compartments shown in Figure 3-30. Strongly opposite to the "with bypass" case, here the simulation pressure rise beside the platinum heater membrane is much higher than measured (~ 35 kPa vs. ~14 kPa). Also of note here is how the measured pressure in the top helium compartment rises rapidly (as fast as the bottom compartment for the first 0.006 seconds) without a thermal lag period. One expects no thermal lag if membrane deflection is the mechanism creating pressure rise but deflection requires a pressure differential.
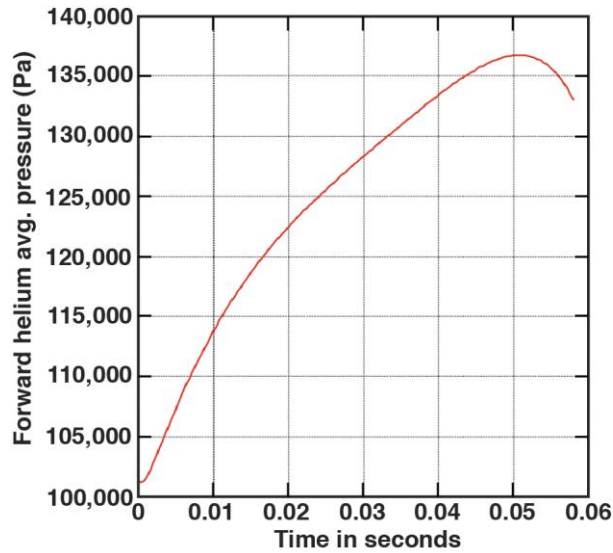
*Figure 3-29. Simulated transient average absolute pressure in the bottom helium compartment of the "without bypass" model*
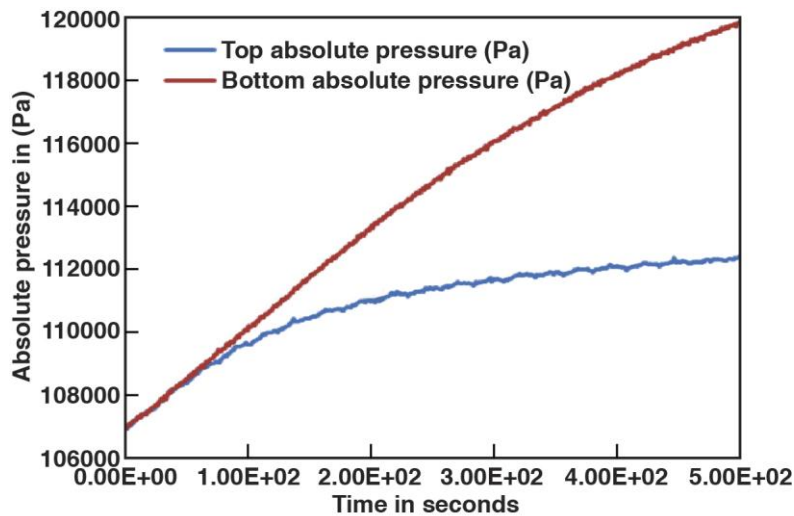


*Figure 3-30. Measured transient absolute pressure in the helium compartments of the "without bypass" test*

The simulation result for the absolute pressure in the top helium compartment is shown in Figure 3-31 below. This result has a time lag of about 0.003 seconds and the magnitude of the response is far lower than that measured for the top compartment (< 1 kPa vs. ~5 kPa). A leak between compartments is only one of several possible explanations for the discrepancy here between test and simulation. Flashing some surface adsorbed molecules during the initial stage of platinum wire heating can contribute to higher than expected pressure response but not fully explain the simultaneous rise of pressure of both helium compartments.  Bulging of the target membranes due to the pressures may also contribute to the discrepancies. The magnitude of the time lag in response of Figure 31, about 0.004 seconds, is of note to more discussion below.
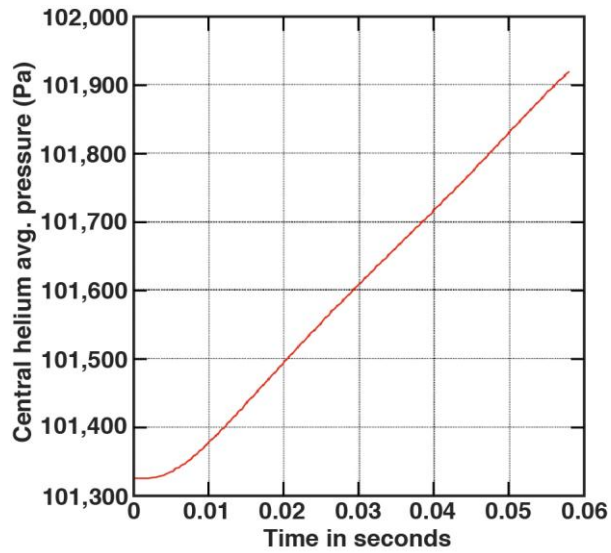
42

*Figure 3-31. Simulated transient average absolute pressure in the central helium compartment of the "without bypass" model*

The simulated transient response of the P2 shield (average temperature) is shown in Figure 3-32 below. The time lag for the P2 shield response is somewhat greater than for the central helium gas compartment and the magnitude of the response is small, only 0.17 Kelvin. The measured response at the P2 shield, shown in Figure 3-33 below, is most likely noise or drift in the sensor, which may be on the order of the simulation result.
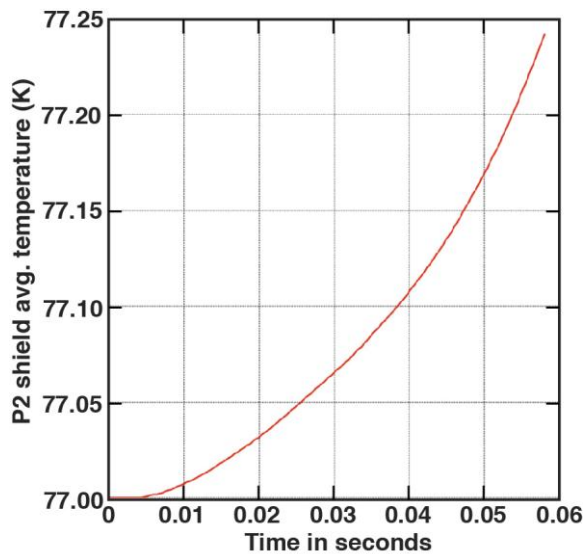


*Figure 3-32. Simulation transient average temperature of the P2 shield of the "without bypass" model*
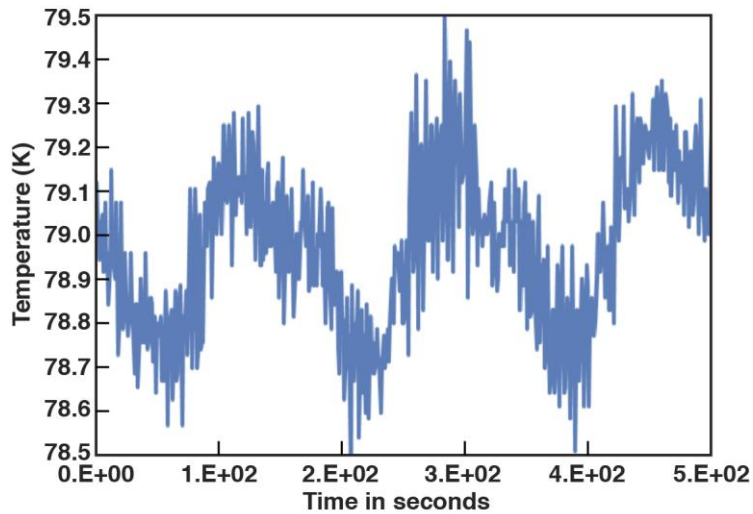
*Figure 3-33. Measured transient of the sensor at the P2 shield of the "without bypass" test*

Simulation transient response at the top membrane is shown in Figure 3-34 below. Both the membrane surface average and maximum temperature are shown in the plot. The temperature rise here is about two thirds that observed for the volume average of the P2 shield although temperature rises are low (<1K).  One might expect the top membrane temperature rise to be a smaller fraction of the P2 shield rise because the top membrane is farther removed from the heating source, but the thermal inertia of the lead is holding its rise down despite the heating helium gas around it. Figure 3-35 below gives the measured transient response of the thermal sensor at the top membrane. This sensor has significant noise in its response and does not show a time lag in response from the test start.  This is unexpected and may result from an error in the test or other some unknown factor.
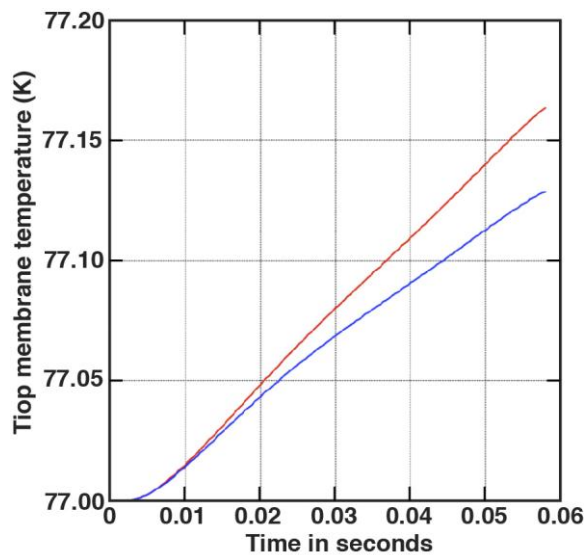


*Figure 3-34. Simulated transient average temperature and maximum temperature of the top membrane of the "without bypass" model*
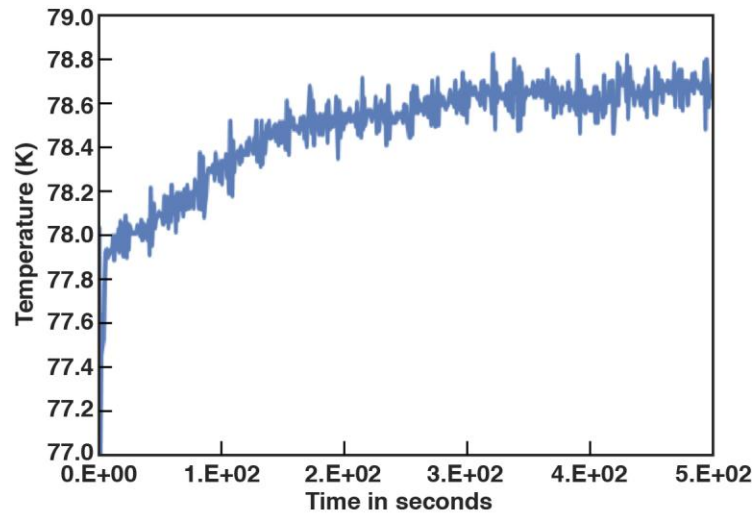
*Figure 3-35, Measured transient temperature at the top membrane of the "without bypass" test*

### 3.6 Conclusion

The tests have shown that the trends expected by the predictions, the increased pressure in the cavity near the LEH window due to heating of the window and the convection currents driving temperature changes in near the IR shield and the compartment near the capsule are confirmed by experiment. More effort is required to determine the causes of the numerical discrepancies between the test values and the models. Since the test values were generally higher than predicted, the predicted values for the fusion target in flight may also be low. The models with "bypass" are closer to predicted. The fusion target will likely require "bypass" to prevent rupture of the membranes. The factor of 2 in actual results over predicted, if that proves to be real, could be accommodated in the actual fusion target using a sacrificial layer on the LEH window which will likely be required.

## 4.0 IR properties of aluminum and carbon thin-films

The reflective layer of aluminum on the 500 nm thick IR shield must be sufficient to block the radiation emanating from the ~900K chamber walls yet be sufficiently thin to not interfere with propagation of either the laser light or the x-rays in the target during the implosion process. The specification is that less than 30 nm of aluminum coating is allowed on the shield. We sought to verify the reflectance of such a thin film at the cold temperatures of interest. In addition, we tested the absorption of carbon-containing thin films as carbon could be a component in either the LEH window or the capsule-support membrane to provide sufficient strength to support the capsule during the acceleration phase of injection. The optical parameters measured in these tests were used in the thermal models of the target flight through the fusion chamber.

### *4.1 Test set-up*

For high-temperature measurements, samples were loaded onto a commercially-available heat stage, the Linkam TS1500 heat stage, capable of heating the sample up to 1500 $^{0}$C at controllable heating rate (Figure 4-1). The stage consisted of a resistively-heated ceramic crucible. The temperature in the crucible was measured in real-time using a thermocouple. Sapphire windows mounted at the top and bottom of the crucible were used to allow both the transmission and reflection of the sample to be measured. The sapphire windows can transmit infrared light up to a wavelength of around 4.5 $\mu$m. The crucible was sealed inside the chamber which was nitrogen-purged to create an inert ambient atmosphere. The exterior of the stage was water-cooled. Infrared data were taken 3 minutes after each temperature point was reached to allow the system to thermally equilibrate between each temperature reading.

Infrared measurements were carried out using a Perkin-Elmer Spectrum 2000 FTIR. This spectrometer was equipped with an infrared microscope, allowing the beam to be focused onto the sample. For graphene, the samples were typically 7mm in diameter. A custom-built stage was made to mount the Linkam sample stage into this microscope setup. Both transmission and reflection (normal-incidence) of the sample could be measured. The microscope-heat stage setup was placed in nitrogen-purged chamber. However, since there were electrical cables and water lines running out of the Linkam stage, the chamber could not be tightly sealed. This resulted in residual gases in the chamber which resulted in peaks appearing in the measurement data due to these residual gases. The lower limit of measurable wavelength was around 2 $\mu$m, limited by the detector in the spectrometer. The upper limit was around 4.5 $\mu$m, limited by the transmission limit of the sapphire windows.

Graphene films were grown by chemical vapor deposition on nickel substrates. The graphene films were then transferred onto sapphire windows 7 mm in diameter. The sapphire window provided an infrared-transparent structural support for the thin graphene film and served to protect the Linkam sample stage from excessive contamination. For high-temperature transmission measurements, the temperature-dependent transmission characteristics of the sapphire window were compensated for as a background signal. The infrared transmission of the sapphire window at various temperatures were measured and

shown in Figure 4-2. This set of data was used to normalize the high-temperature transmission data of graphene.

For low-temperature infrared measurements of thin aluminum film on glass substrate, samples were loaded into a commercially-available cold stage, the Linkam THMS 600 temperature-controlled stage, capable of cooling the sample down to liquid nitrogen temperature of -197 $^0$C at controllable rate (Figure X). The cooling was achieved by flowing liquid nitrogen beneath the sample stage. Real-time temperature in the crucible was obtained by a thermocouple.

### 4.2 Test results

The measured temperature dependent IR transmission of a 1000 nm thick polyimide film is shown in Figure 4-3.  As the temperature is increased from room temperature to 200 $^0$C, the film's IR transmission is decreased by around 10 %.

For a 100 nm graphene film, the IR transmission decreases from 10 % to 8 % as the temperature is varied from room temperature to 1300 $^0$C (Fig. 4-4). After cooling back down to room temperature, the IR transmission largely recovers to its original value. This result shows that the graphene film has excellent thermal stability. The IR reflectance of the film decreases from around 40 % to 20 % as temperature varies from room temperature to 1300 $^0$C. We can thus deduce that the IR absorption (assuming no scattering) increases from 50 % to 70 % during this thermal test.

For a 30 nm aluminum film, it is verified that the film maintains a high IR reflectance of above 90 % down to liquid nitrogen temperature (Fig. 4-5).

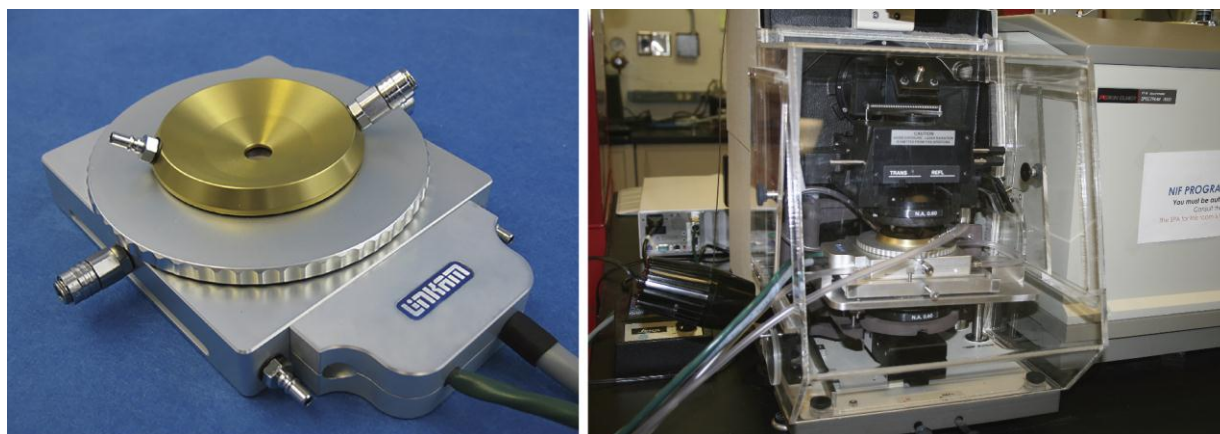The values for the reflected radiation off the aluminized film were used in the calculations cited in Table 1-1.



*Figure 4-1. Experimental Setup for IR characterization of polyimide, graphene and aluminum films*
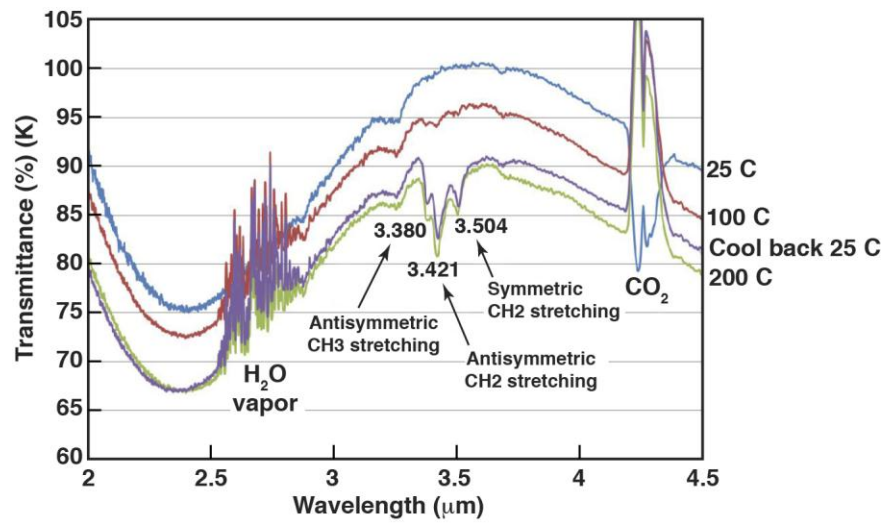
*Figure 4-2. Measured transmission of 1000 nm thick polyimide at room temperature*
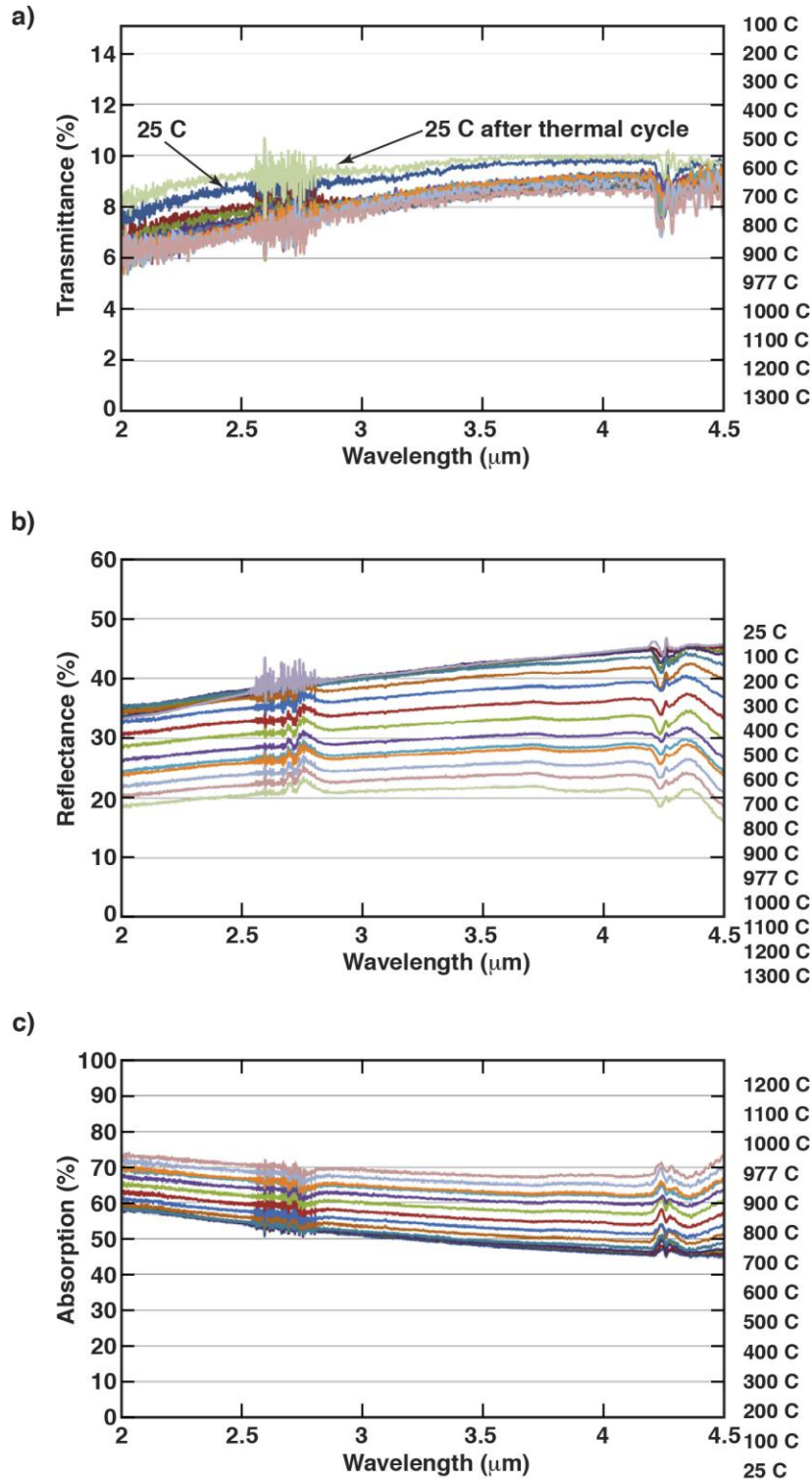
*Figure 4-3. Measured transmission (a) reflection (b) and calculated absorption (c) of 100nm thickness graphene as a function of temperature*
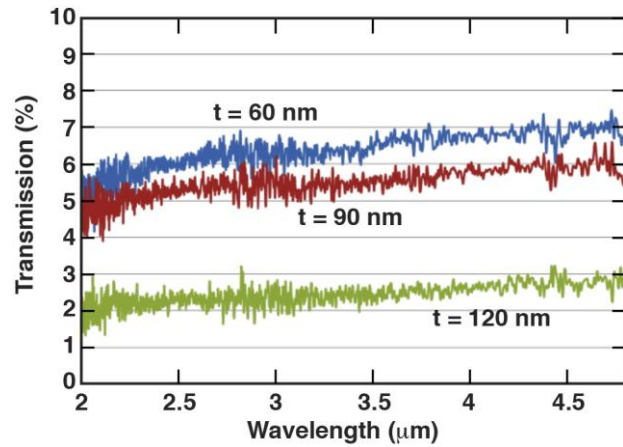
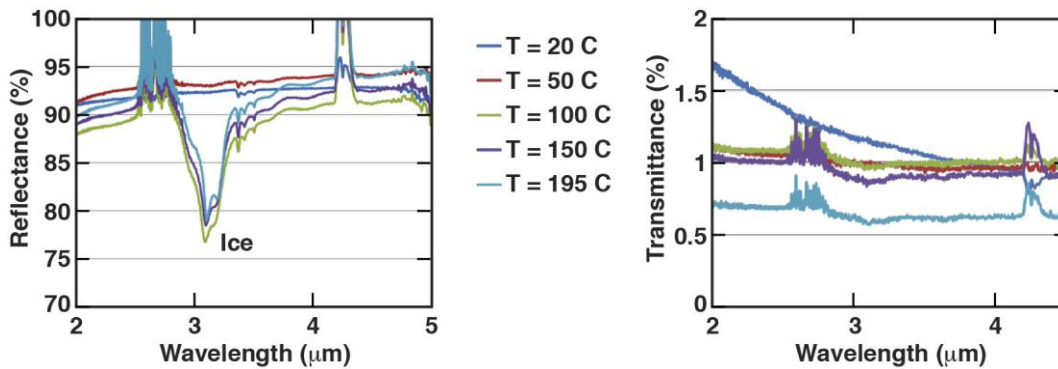*Figure 4-4. Transmission of graphene as a function of thickness*



*Figure 4-5. Measured reflection/transmission of 30 nm aluminum on a glass substrate as a function of temperature*

## 5.0 Conclusion

The tests of the external heat transfer coefficient suggests that the values used in the numerical analysis for the temperature distribution within the fusion fuel target following flight into the target chamber are probably valid.  The tests of the heat transfer phenomena occurring within the target due the rapid heating of the LEH window for the hot gasses within the fusion chamber show that the heat does indeed convect via the internal helium environment of the target towards the capsule and that the pressure in the front compartment of the target adjacent to the LEH window  increases such that t bypass venting of the internal helium into the second chamber  adjacent to the capsule is needed to prevent rupture of the membranes.   The bypass flow is cooled by the hohlraum during this venting.  However, the experiments suggest that our internal heat flow calculations may be low by about a factor of 2.  Further studies need to be conducted to investigate the differences between the experiment and the numerical analysis.  Future studies could also possibly bring the test conditions closer to those expected in the

fusion chamber to better validate the results.  A sacrificial layer will probably be required on the LEH window of the target and this can be used to mitigate any unexpected target heating.